OULU 2022
C 854

ACTA UNIVERSITATIS OULUENSIS


*Rita Kallio*

# MULTIDISCIPLINARY STUDY OF THE BENEFICIATION POTENTIAL OF THE KIVINIEMI FERROUS SCANDIUM DEPOSIT

*UNIVERSITY OF OULU GRADUATE SCHOOL;*
*UNIVERSITY OF OULU,*
*FACULTY OF TECHNOLOGY*

ACTA UNIVERSITATIS OULUENSIS
C Technica 854

*RITA KALLIO*

# MULTIDISCIPLINARY STUDY OF THE BENEFICIATION POTENTIAL OF THE KIVINIEMI FERROUS SCANDIUM DEPOSIT

Academic dissertation to be presented, with the assent of the Doctoral Programme Committee of Technology and Natural Sciences of the University of Oulu, for public defence in Auditorium IT116, Linnanmaa, on 2 December 2022, at 1 p.m.

UNIVERSITY OF OULU, OULU 2022

Acta Univ. Oul. C 854, 2022

Supervised by
Professor Saija Luukkanen
Professor Timo Fabritius
Professor Ulla Lassi

Reviewed by
Associate Professor Hesham Ahmed
Professor Alan Butcher

Opponent
Professor Pertti Lamberg

ISBN 978-952-62-3492-2 (Paperback)
ISBN 978-952-62-3493-9 (PDF)

ISSN 0355-3213 (Printed)
ISSN 1796-2226 (Online)

Cover Design
Raimo Ahonen

PUNAMUSTA
TAMPERE 2022

**Kallio, Rita, Multidisciplinary study of the beneficiation potential of the Kiviniemi ferrous scandium deposit.**

University of Oulu Graduate School; University of Oulu, Faculty of Technology
*Acta Univ. Oul. C 854, 2022*
University of Oulu, P.O. Box 8000, FI-90014 University of Oulu, Finland

## *Abstract*

The European Union lacks domestic primary production of scandium (Sc); therefore, this metal is currently classified as a critical raw material with a very limited, highly concentrated supply base. Finding new Sc sources would create a foundation for a more stable market, decrease the dependency on non-European suppliers and increase the use of Sc in high-technology applications.

To respond to the lack of supply, potential primary and secondary resources of Sc are being investigated. The recently discovered Sc deposit associated with the Kiviniemi mafic intrusion in eastern Finland has a preliminary mineral resource estimate of 13.4 Mt with an average Sc grade of 163 g/t, allowing for regarding Kiviniemi as a potential Sc deposit. The Kiviniemi intrusion has high Sc, Fe, Ti, and P contents, with Sc being mainly incorporated into the lattices of ferrous clinopyroxene and amphibole. To release Sc from ferrous silicates, the following 3-stage processing scheme has been suggested: 1) magnetic separation to decrease the amount of alkali-containing diamagnetic minerals and produce ferrous concentrate enriched in Sc; 2) pyrometallurgical reduction of the ferrous component from the magnetic concentrate, and 3) hydrometallurgical extraction of Sc from FeO-depleted and $Sc_2O_3$-enriched slag. The purpose of thesis was to conduct experimental investigations on suggested processing steps, supplemented with material characterization.

A combination of low-intensity (LIMS) and high-gradient magnetic separation (HGMS) with SLon® resulted in 32–45 mass% reduction from the feed and only negligible losses of $Sc_2O_3$ to the tailings. The characteristics of the reduction of the ferrous oxide component from the magnetic preconcentrate were investigated using thermogravimetric analysis (TGA). Moderate additions of CaO were shown to improve the reduction characteristics and segregation of metallic iron from the $Sc_2O_3$-enriched slag. The resulting acidic, amorphous slag was submitted to $H_2SO_4$-based leaching experiments. Although the risk of gelation was avoided by the mentioned methods, the efficiency of leaching remained at best at the level of 40−50%. However, the obtained results provide a foundation for further investigations on the beneficiation possibilities of Kiviniemi-type ferrous scandium deposits. Further studies could include modification of slag properties to improve the potential for selective leaching and/or further investigations of the direct hydrometallurgical extraction of Sc from the concentrates, provided a control over Fe dissolution could be established.

*Keywords:* hydrometallurgy, Kiviniemi deposit, magnetic separation, process mineralogy, pyrometallurgy, scandium

**Kallio, Rita, Monitieteinen tutkimus Kiviniemen rautapitoisen skandiumesiintymän hyödyntämismahdollisuuksista.**
Oulun yliopiston tutkijakoulu; Oulun yliopisto, Teknillinen tiedekunta
*Acta Univ. Oul. C 854, 2022*
Oulun yliopisto, PL 8000, 90014 Oulun yliopisto

## *Tiivistelmä*

Skandium on EU:n luokittelun mukaan ns. kriittinen raaka-aine, jolla on kohtalainen tai korkea taloudellinen merkittävyys ja Euroopan teollisuuden kannalta saatavuusriski. Sen kysynnän odotetaan kasvavan merkittävästi lähitulevaisuudessa korkean teknologian käyttökohteissa.

Kiviniemen skandiumesiintymä on EU:n alueella merkittävä potentiaalinen raaka-ainelähde odotusarvoltaan kasvaville Sc-markkinoille. GTK:n alustavan malmiarvion mukaan se sisältää 13,4 miljoonaa tonnia skandiumpitoista kiveä, jossa keskipitoisuus on 163 g/t skandiumia. Skandium on Kiviniemen mineralisaatiossa sitoutunut rautapitoisten silikaattimineraalien, pyrokseenin ja amfibolin kidehilaan. Kiviniemen-tyyppisen lähtömateriaalin prosessoimiseksi on ehdotettu kolmivaiheista menetelmäketjua: 1) malmi rikastetaan perinteisillä magneettisilla menetelmillä pyrokseeni-amfibolirikasteeksi; 2) korkean rautapitoisuuden vuoksi rikasteen sisältämä rautaoksidikomponentti pelkistetään pyrometallurgisin menetelmin metalliseksi raudaksi skandiumin konsentroituessa kuonafaasiin; 3) skandium liuotetaan tuotetusta kuonasta. Tässä tutkimuksessa selvitettiin kokeellisesti ehdotettuihin vaiheisiin liittyviä ilmiöitä sekä karakterisoitiin tuotettuja materiaaleja.

Magneettisilla erotusmenetelmillä pystytään poistamaan merkittävä määrä (32–45 massa-%) alkaleja sisältäviä, diamagneettisia harmemineraaleja skandiumin saannin pysyessä korkealla tasolla. Tuotetun, rautapitoisen rikasteen pelkistystutkimuksissa todettiin maltillisen CaO-lisäyksen parantavan metallisen raudan erottumista happamasta kuonasta. Happaman ja amorfisen $Sc_2O_3$-pitoisen kuonan liuotusprosessin haasteina on estää piihappogeelin muodostuminen; käytetyillä $H_2SO_4$-pohjaisilla menetelmillä geelin muodostuminen vältettiin, mutta skandiumin saanti liuokseen jäi 40–50 %:iin. Tutkimus on kuitenkin tuottanut lisää hyödyllistä tietoa Kiviniemen-tyyppisen materiaalin hyödyntämisvaihtoehtojen kartoittamiseen. Jatkotutkimuksissa voitaisiin tarkastella joko sulapelkistyksellä muodostetun kuonan lisämodifiointia liuotuksen selektiivisyyden parantamiseksi, ja/tai selvittää mahdollisuuksia rikasteen hydrometallurgiselle prosessoinnille, mikäli raudan liukeneminen ja sen erotus saataisiin hallintaan.

*Asiasanat:* hydrometallugia, Kiviniemen esiintymä, magneettierotus, prosessimineralogia, pyrometallurgia, skandium

# Acknowledgements

The original idea of investigating the Kiviniemi deposit, which has a relatively high content of an element with profound challenges in terms of geological enrichment and technical beneficiation potential, was presented by Pekka Tanskanen, whose support and positive encouragement enabled the execution and completion of this study. One important aspect of this study was the close collaboration between three research units at the Faculty of Technology, University of Oulu, which started with magnetic separation experiments at the Oulu Mining School, followed by high-temperature experiments in the Process Metallurgy unit, and finalized by leaching studies in the Sustainable Chemistry unit. The execution of this type of study in collaboration of three research units, though not necessarily the easiest for administration, hopefully demonstrates the possibilities of multidisciplinary case study, and I am grateful to all three professors, Saija Luukkanen, Timo Fabritius and Ulla Lassi to allow this to happen. Furthermore, all three professors took a firm grip toward the end of this project to support and guide in finalizing this thesis.

For its main part (2019–2021), this research was funded by the Foundation for Research of Natural Resources in Finland with additional funding in 2022 from the K. H. Renlund Foundation. Strong support from Dr. doc. Tapio Halkoaho (Geological Survey of Finland), providing access to drill core samples, and from Dr. doc. Jussi Liipo (Metso Outotec), enabling magnetic separation experiments, both being members of the follow-up steering group and taking the responsibility for chairing the steering group at the final stage of this study, is highly appreciated. The chairman of the research follow-up group for the main part of the study, Dr. doc. Eetu-Pekka Heikkinen, provided valuable support and expertise throughout the project. Comments from Professor Emer Eero Hanski throughout the progression of the study are gratefully acknowledged. Help in practical work provided by Sari Forss, Tommi Kokkonen, Eveliina Holappa, Toni Kauppinen, Dr. Janne Pesonen and Mika Cristophliemk are highly appreciated. The professional help from the personnel at the Center for Material Analysis was the key to conducting material characterization—a crucial part of this study. Highly necessary dosages of both sugar and laughs were provided by the Perjantaipullat group throughout the study. Ultimately, this thesis would not have happened without my family and friends.

02.12.2022 Rita Kallio

# List of abbreviations and symbols

| | |
|---|---|
| $\alpha$ | degree of conversion |
| AM | amphibole |
| AP | apatite |
| aq | aqueous |
| BT | biotite |
| CAL | calcite |
| $c_i$ | metal concentration in the leaching solution |
| *CC* | concentration criterion |
| *Cc* | concentrate mass and assay |
| CEF | compound energy formalism |
| CFGC | Central Finland Granitoid Complex |
| CFS | clinoferrosilite |
| CHL | chlorite |
| CMA | Centre for Material Analysis |
| CPX | clinopyroxene |
| D | partition coefficient |
| $D_f$ | density of fluid |
| $D_h$ | density of heavy particles |
| $D_l$ | density of light particles |
| DMS | dense media separation |
| EPMA | electron probe microanalyzer |
| $\eta i$ | leaching efficiency |
| FA | fayalite |
| FeOx | iron oxides |
| FESEM | field emission electron microprobe |
| FSP | potassic feldspar |
| GPa | gigapascal |
| GRT | garnet |
| GTK | Geological Survey of Finland |
| HEA | high-entropy alloy |
| HFSE | high-field strength element |
| HPAL | high-pressure acid leaching |
| HPC | high-pressure caustic leach |
| HSAB | hard-soft-acid-base |
| HPOXAL | high-pressure oxidative acid leaching |

| | |
|---|---|
| ICP-OES | inductively coupled plasma optical emission spectrometry |
| ILM | ilmenite |
| JORC | Joint Ore Reserves Committee |
| LBM | laser beam manufacturing |
| LIMS | low intensity magnetic separation |
| $m$ | sample mass |
| $m_0$ | initial sample mass for TG experiment |
| $m_f$ | sample mass at the end of the experiment |
| M1 site | smaller octahedral site in pyroxene structure |
| M3 site | octahedral site in amphibole structure |
| NSR | net smelter return |
| NYF | Nb-Y-F pegmatites |
| PHGMS | pulsating high gradient magnetic separator |
| PL | plagioclase |
| PLS | pregnant leach solution |
| QTZ | quartz |
| $R$ | recovery |
| REE | rare earth elements |
| RM | red mud |
| SDD | silicon drift detector |
| SEM | scanning electron microscope |
| S/L | solid to liquid ratio |
| SOFC | solid oxide fuel cell |
| SULF | sulfides |
| $T$ | temperature |
| $t$ | time |
| TREE | total rare earth elements |
| $Tt$ | tailings mass and assay |
| µm | micrometer |
| nm | nanometer |
| pm | picometer |
| $V$ | volume of leaching solution |
| WHIMS | wet high-intensity magnetic separation |
| $x_i$ | mass fraction of the metal element in the slag |
| $X$ | variable ($T$, $t$) |
| XRD | X-ray diffraction |
| ZRN | zircon |

# List of original publications

This thesis is based on the following publications, which are referred to by their Roman numerals throughout the text:

I Kallio, R., Tanskanen, P., & Luukkanen, S. (2021). Magnetic preconcentration and process mineralogical study of the Kiviniemi Sc-enriched ferrodiorite, eastern Finland. *Minerals, 11*, 966. https://doi.org/10.3390/min11090966.

II Kallio, R., Tanskanen, P., Heikkinen, E. P., Kokkonen, T., Luukkanen, S., & Fabritius, T. (2022). Reduction characteristics of Kiviniemi ferrous scandium concentrate. *Minerals Engineering, 177*, 107369. https://doi.org/10.1016/j.mineng.2021.107369.

III Kallio, R., Tanskanen, P., Heikkinen, E. P., Kokkonen, T., Luukkanen, & S., Fabritius, T. (2022). Slag modification in reduction of Kiviniemi ferrous scandium concentrates. *Metals, 12*, 709. https://doi.org/ 10.3390/met12050709.

IV Kallio, R., Lassi, U., Kauppinen, T., Holappa, E., Christophliemk, M., Luukkanen, S., Tanskanen, P., & Fabritius, T. (2022) Leaching characteristics of Sc-enriched, Fe-depleted acidic slags. *Minerals Engineering, 189*, 107901. https://doi.org/10.1016/j.mineng.2022.107901.

Rita Kallio is the main author of all mentioned publications (I–IV), and she has written the original drafts. She has taken responsibility for the conceptualization, planning and conducting of experiments, characterization, analysis and visualization of data.

# Contents

# 1 Introduction

There is no domestic primary production of scandium (Sc) in the European Union; therefore, this metal is currently classified as a critical raw material with a very limited, highly concentrated supply base (Blengini et al., 2020). Hence, new Sc sources are required that can provide the foundation for a more stable market and help increase the use of scandium in high-technology applications (Bobba et al., 2020; Blengini et al., 2020). To respond to the lack of Sc supply and its expected increasing demand, potential new sources of Sc are investigated from various primary and secondary resources (Botelho Junior et al., 2021). One example of potentially exploitable Sc mineralization is the recently discovered Sc deposit associated with the Kiviniemi mafic intrusion in eastern Finland, which has a preliminary mineral resource estimation of 13.4 Mt, with an average Sc grade of 163 g/t (Halkoaho et al., 2020; Hokka & Halkoaho, 2016).

Based on preliminary metallurgical tests with samples collected from the Kiviniemi intrusion during 2009–2010 (Korhonen et al., 2011), magnetic separation resulted in a mineral concentrate with ~346 ppm Sc at a recovery level of ~72%; therefore, it was suggested to be the most potential concentration method for Sc-bearing minerals of the deposit. Using a mixture of hydrogen fluoride and hydrochloric/sulfuric acid in leaching experiments resulted in the best dissolution of Sc, but the solubility of Fe was almost 1000-fold in comparison with Sc. Furthermore, this type of processing required large quantities of acids and produced large volumes of materials that needed to be managed in further processing (Korhonen et al., 2011).

To overcome the harmful issues introduced by Fe to the hydrometallurgical processing of concentrate, a three-stage processing scheme is suggested for Kiviniemi-type deposits (Figure 1). It introduces a preconcentration stage with conventional magnetic methods followed by pyrometallurgical treatment to reduce the ferrous oxide component prior to hydrometallurgical processes. This study was designed to experimentally investigate the main features related to each of the suggested processing stages, as illustrated in Figure 1. The purpose of this study was to identify the related physical and chemical phenomena supplemented with mineralogical and chemical characterization of Kiviniemi-type feed material along the progression of work from one stage to another. Paper I presents the results on the magnetic separation stage and the process mineralogical details of the samples included in this study. Papers II and III focus on the high-temperature reduction characteristics of the concentrates produced. Finally, Paper IV completes the

original research plan by presenting the first sets of hydrometallurgical extraction experiments on $Sc_2O_3$-enriched and FeO-depleted slag.

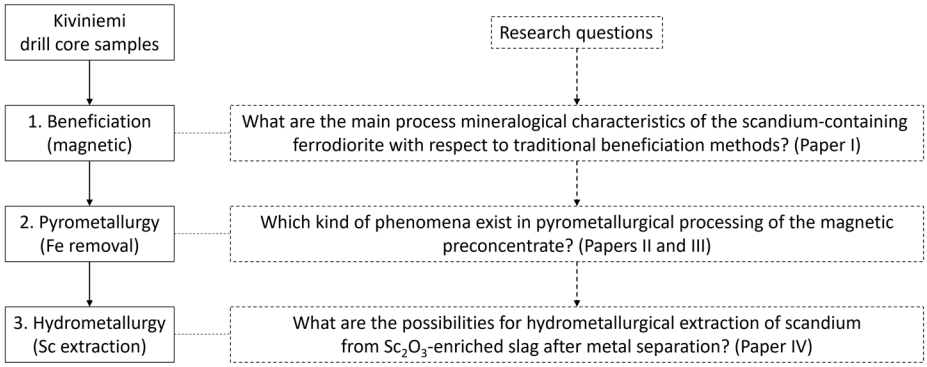


**Fig. 1. Research questions and the progression of work with the produced articles.**

# 2 Scandium

Scandium has an atomic number of 21 and atomic mass of 44.96. It was discovered in 1879 by Swedish chemist L. F. Nilson when he was trying to isolate ytterbium from minerals gadolinite and euxenite (Gupta & Krishnamurthy, 2005; Horovitz, 1975). Although Nilson was not able to complete the examination of the chemical properties of this new element due to its very limited amount, he was still able to determine the atomic mass of Sc and the density of its oxide. He named this new element scandium in honor of Scandinavia (lat. Scandia). After its discovery, little attention was paid to scandium for decades. Scandium metal itself was produced for the first time in 1937 by the electrolysis of molten scandium chloride (Horovitz, 1975).

Scandium is placed in group 3 (IIIB) of the periodic table with an electronic configuration of $[Ar]3d^14s^2$ and, in nature, occurs exclusively as $^{45}Sc$; it has an oxidation state of +3 and an electronegativity of 1.36 (Williams-Jones & Vasyukova, 2018). It has a high charge to radius ratio and is a hard cation in hard-soft-acid-base (HSAB) terminology (Pearson, 1963). Accordingly, it tends to form strong aqueous complexes with hard ligands, such as $OH^-$ and $F^-$ (Williams-Jones & Vasyukova, 2018; Wood & Samson, 2006).

Scandium and yttrium are classified as rare earth elements (REE) together with the fifteen lanthanides (Connelly et al., 2005; Sahama, 1947), although sometimes scandium may also be excluded from the REE (Henderson, 1984; Jordens et al., 2013). This is due to its smaller ionic radius (Figure 2) (Sc 75 pm in octahedral coordination while lanthanides range from 103 to 86 pm; Henderson, 1984; Shannon, 1976). Consequently, in geological systems, Sc behaves differently from the rest of the group. Despite being a trivalent cation, the relatively small ionic radius of Sc makes it a moderately compatible element fitting into the lattice of common ferromagnesian rock-forming minerals, particularly pyroxene, amphibole and garnet (Williams-Jones & Vasyukova, 2018). The substitution of Sc for Mg or Fe in the M1 octahedral site in clinopyroxene is possible due to the similarity of the ionic radius of $Sc^{3+}$ with those of $Mg^{2+}$ and $Fe^{2+}$ (72 and 78 pm respectively); Sc is also suggested to enter the M3 site in the amphibole structure (Horovitz, 1975; Samson & Chassé, 2016).

In the bulk continental crust the average Sc abundance is 22 ppm (Taylor, 1964). Mafic igneous rocks contain 30-40 ppm scandium on average, whereas the abundance is less than 20 ppm in felsic rocks (Norman & Haskin, 1968 as cited in Halkoaho et al., 2020).

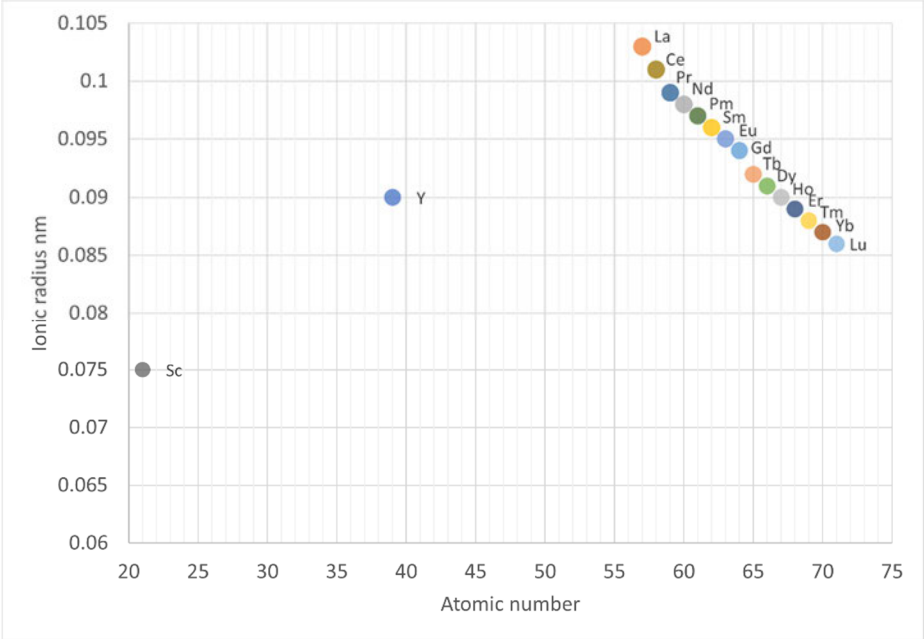


**Fig. 2. The ionic radii of the trivalent lanthanides, yttrium, and scandium (Shannon, 1976). The systematic decrease in the size of lanthanide ions with an increase in atomic number is called lanthanide contraction. Yttrium is considered one of the "heavy" rare earth elements, whereas scandium is often excluded from the rare earth element grouping due to its much smaller ionic radius.**

## 2.1 Scandium deposits

As a lithophile element, scandium is widely dispersed in the lithosphere, residing predominantly in silicate minerals rather than in metal- or sulfur-bearing minerals (Henderson, 1984; Jaireth et al., 2014). The bulk of the element is contained in rocks formed in the early stages of magmatic differentiation, although, to some extent, it may also pass through to late stages of differentiation, entering pegmatites and pneumatolytic and hydrothermal deposits (Horovitz, 1975; Sahama, 1947).

Only a few rare minerals are known to possess Sc as a major constituent. These include thortveitite ($Sc_2Si_2O_7$), pretulite ($ScPO_4$), kolbeckite ($ScPO_4{\cdot}2H_2O$), jervisite ($NaScSi_2O_6$), eringaite ($Ca_3Sc_2(SiO_4)_3$), bazzite ($Be_3Sc_2Si_6O_{18}$), heftetjernite ($ScTaO_4$), juonniite ($CaMgSc(PO_4)(OH){\cdot}4(H_2O)$) and cascandite ($CaScSi_3O_8(OH)$), which are commonly hosted in granitic pegmatites, quartz veins

or phosphate deposits (Horovitz, 1975; Williams-Jones & Vasyukova, 2018). In addition to actual scandium minerals, scandium may be present in significant proportions in a number of high field strength element (HFSE) minerals, such as columbite, tantalite, and ixiolite, and in titanium and zirconium minerals, and it may also be present as a trace constituent in ferromagnesian silicate minerals (Williams-Jones & Vasyukova, 2018).

According to Walters et al. (2011), the geological formations in which REE, including Sc, are enriched can be broadly divided into primary Sc deposits related to igneous and hydrothermal processes and secondary deposits where sedimentary processes and weathering concentrate Sc to produce laterite and placer deposits. A similar classification based on geological enrichment processes was suggested by Wang et al. (2021), who distinguished magmatic, hydrothermal, and supergene scandium deposits. Magmatic and post-magmatic processes concentrate Sc in minerals, such as clinopyroxene, amphibole and baddeleyite, in addition to actual Sc-minerals, such as thortveitite and Sc-rich phosphates. Wang et al. (2021) estimated that magmatic deposits (mafic–ultramafic intrusions) constitute to about 90% of the global Sc resources, hosted mainly in clinopyroxene ± amphibole.

As stated by Williams-Jones and Vasyukova (2018), the main magmatic processes with respect to Sc concentration are partial melting and fractional crystallization. The nature of the source and the degree of partial melting control the composition of the primitive melts, which may be key factors in determining the Sc concentrations of igneous rocks (Wang et al., 2021). According to Chassé et al. (2018), garnet accounts for ~75% of the Sc budget of the deep lithospheric mantle, controlling the mobility of Sc. Because of the incompatibility of Sc in spinel but its high compatibility in garnet, the behavior of Sc during partial melting of the mantle is largely influenced by the relative proportions of spinel and garnet in the source (Chassé et al., 2018; Wang et al., 2021). At high pressures (>3 GPa), most Sc is hosted in garnet, whereas at lower pressures (<2 GPa) in the spinel peridotite facies of the upper mantle, Sc is mainly hosted in clinopyroxene (Li, 2018; Wang et al., 2021).

Considering mineral-melt partitioning of trace elements in magmatic systems, the values of partition coefficients (D) are dependent not only on P-T but also on crystal chemistry, melt composition, and melt water content (Bédard, 2014; Hill et al., 2011; Li, 2018). Clinopyroxene and amphibole both have moderately high $D_{Sc}$ values, which are principally controlled by the MgO content of the melt, with D increasing with decreasing MgO (Bédard, 2014; Williams-Jones & Vasyukova, 2018). With respect to $D_{Sc}^{Cpx/silicate\ melt}$, scandium is insensitive to the variation of

mantle $fO_2$ due to a valence state of $3^+$ at Earth's upper mantle conditions (Li, 2018; Mallmann & O'Neill, 2009).

Clinopyroxenites in the Alaskan-type intrusions are mentioned as examples of having a high potential for Sc resources due to the preference of clinopyroxene to host Sc (Wang et al., 2021). In their experimental study of fractional crystallization of an anhydrous mantle-derived tholeiitic magma at 1.0 GPa, Villiger et al. (2004) observed coprecipitation of clinopyroxene and orthopyroxene, whereas in the experiments conducted by Nandedkar et al. (2014) at 0.7 GPa using calc-alkaline to tholeiitic magmas, clinopyroxene crystallized under hydrous conditions with only minor orthopyroxene within a narrow temperature range. Therefore, the formation of Sc-rich clinopyroxene and suppression of the crystallization of orthopyroxene could be favored by involvement of water (Wang et al., 2021), as commonly observed in the Alaskan-type mafic–ultramafic intrusions (Thakurta, 2018). Alaskan-type mafic–ultramafic intrusions, such as those in the Ural Mountains in Russia, have been reported to host Sc-rich clinopyroxenite ± hornblendite, with Sc contents in clinopyroxenite ranging from 78 to 135 ppm (Krause et al., 2007). Furthermore, ultramafic-mafic intrusions in the Zhongtiao Mountain region in China host hornblendite with 71–78 ppm Sc (Yuan et al., 2017). Alaskan-type complexes have been interpreted as products of fractional crystallization of magmas originating from mantle plumes, similar to those forming continental flood basalts (Ishiwatari & Ichiyama, 2004; Pirajno et al., 2008; Williams-Jones and Vasyukova, 2018). Although most Alaskan-type complexes occur in convergent tectonic settings, or in mobile belts, in broader terms these types of complexes can be considered to represent volcanic flow-through systems and magma storage reservoirs regardless of their tectonic settings (Thakurta, 2018).

In addition to mafic–ultramafic intrusions, carbonatite, and alkaline rock complexes are known to host Sc-rich minerals; however, the enrichment mechanisms remain unclear. According to the melt-melt-partitioning data obtained from carbonate-silicate systems, Sc partitions strongly into the silicate melt in anhydrous carbonate systems and weakly favors the carbonate phase in a hydrous system (Martin et al., 2013; Williams-Jones & Vasyukova, 2018). In the Bayan Obo REE-Nb-Fe deposit in China, carbonatitic magma has been suggested to be the likely source of scandium, although scandium is concentrated mainly in clinopyroxene of a metasomatic origin (Fan et al., 2016; Zhou et al., 2017; Williams-Jones & Vasyukova, 2018). In addition to aegirine, a small proportion of scandium is also hosted at Bayan Obo in bastnäsite, monazite and fluorite, which are all interpreted to have formed because of the interaction of hydrothermal fluids

with dolomitic rocks. The Zhovti Vody deposit in Ukraine also hosted metasomatic aegirine enriched in Sc (Williams-Jones & Vasyukova, 2018).

In the case of the Kovdor baddeleyite-magnetite-apatite deposit in the Kola Alkaline Province, NW Russia, Sc has been enriched in a P-rich basic alkaline magma (phoscorite) as well as carbonatite magma and is incorporated in baddeleyite (Kalashnikov et al., 2016). The exact process of Sc enrichment is not known; however, it potentially involves the following coupled substitution: $2Zr^{4+} \leftrightarrow Nb^{5+} + Sc^{3+}$. One of the world's largest carbonatites, Tomtor in Russia (Lapin et al., 2016) has elevated contents of REEs, including scandium, but the concentration to exploitable levels is the result of post-magmatic weathering. A resource of ~100 Mt of ore grading 390 ppm Sc has been established, with the occurrence of Sc being restricted mainly to xenotime (-Y) (Williams-Jones & Vasyukova, 2018).

The Crater Lake syenitic intrusion (formerly also known as Misery Lake; Beland, 2021) in northern Quebec, Canada, hosts a potentially important REE-Zr-Nb prospect, containing significant contents of both light and heavy REEs (Petrella et al., 2014). Syenitic intrusion is mainly composed of early ferrosyenite and late felsic syenite units, of which the former contains up to 50 vol% of ferromagnesian minerals including fayalite, hedenbergite, ferropargasite and Ti-rich magnetite with up to 1–2 vol% of primary zircon and fluorapatite (Petrella et al., 2014). The ferrosyenite is interpreted to have formed by fractional crystallization of ferromagnesian minerals, evolving into a residual magma which produced the felsic syenites. Gravitational settling of fluorapatite initially concentrated the bulk of the REE mineralization. High abundance of Sc is restricted to the ferrosyenite, with the grades ranging from 150 to 300 ppm (Williams-Jones & Vasyukova, 2018), though locally reaching 1000 ppm (Petrella et al., 2014), with most of Sc being hosted in hedenbergitic clinopyroxene at a general content of 800 ppm (Wang et al., 2021).

Enrichment of Sc is occasionally found in late stages of magmatic processes producing pegmatites and pneumatolytic-hydrothermal formations, involving preconcentration of Sc in the late-stage liquid and precipitation of Sc-rich minerals at favorable physicochemical conditions. In addition to partitioning of Sc into late-stage exsolved liquids, mobilization from earlier crystallized Sc-bearing minerals, and scavenging from Sc-rich wall rocks are mentioned as possibilities for Sc enrichment (Wang et al., 2021). The ability of Sc to form fluoride complexes and the segregation of melt enriched in fluorides may be connected to Sc enrichment (Gramaccioli et al., 2000; Shchekina & Gramenitskii, 2008). Thorveitite-bearing NYF pegmatites in Evje-Iveland in Norway were exploited for Sc from the early

20th century to 1960s (Williams-Jones & Vasyukova, 2018). Other occurrences of Sc-bearing pegmatites include the Befanamo deposit in Madagaskar, the Crystal Mountain deposit in USA, the Baveno and Cuasso al Monte deposits in Italy, and the Yingjiang deposit in China (Wang et al., 2021). According to the recent study of the Evje–Iveland pegmatites by Gion et al. (2021), they are proposed to be the result of partial melting of a Sc-rich ultramafic or mafic complex, differentiation of the formed melt, and emplacement of the residual melt into the host amphibolites. Thus, the currently preferred model for the origin of the Evje–Iveland pegmatites involves their formation in the final stages of magmatic differentiation (Gion et al., 2021).

Lateritic Sc deposits are considered a viable source for future scandium production (Williams-Jones & Vasyukova, 2018). The most important of them are located in Australia; JORC-determined resources of Ni, Co, and Sc include the Lucknow and Greenvale deposits in Queensland and the Nyngan and Syerston deposits (currently known as the Sunrise project) in New South Wales (Jaireth et al., 2014; Rangott et al., 2016). Deeply weathered laterite profiles have been developed above Phanerozoic mafic–ultramafic intrusions, which have been variously described in the literature as having an ‘alpine’-, ‘ophiolite’-, and ‘Alaskan’-type affinity (Jaireth et al., 2014). During the weathering of primary mafic minerals, Sc is released into solution with subsequent transportation and redeposition and/or adsorption on clay minerals (Horovitz, 1975). A four-stage model has been proposed for the mobility and concentration of Sc during the formation of Sc-rich sedimentary profiles (Chassé et al., 2019). According to this model, the initial Sc reservoir of an ultramafic or mafic intrusion provides the source for the formation of Sc-bearing smectitic clays, formed by dissolution of clinopyroxene. These clays immobilize and concentrate Sc by topotactic replacement under reducing conditions. After smectite dissolution, iron oxides and oxyhydroxides scavenge Sc by adsorption, which is further concentrated by the successive dissolution-recrystallization of goethite generations, eventually resulting in a Sc-enriched lateritic duricrust (Chassé et al., 2017; Chassé et al., 2019).

In summary, considering igneous rocks, the relatively low contents of Sc in basaltic melts coupled with its moderately compatible nature, promotes the dispersion of Sc into ferromagnesian minerals at the early stages of crystallization. Scandium is not easily enriched by geological processes to ore grades due to the geochemical characteristics which are controlled largely by its ionic charge and ionic radii. Consequently, the estimated global Sc production is only 15 to 25 tpa

(Chassé et al., 2017; Eilu, 2017; U.S.Geological Survey, 2022; Williams-Jones & Vasyukova, 2018). Main features of selected Sc deposits are summarized in Table 1, including both those that are currently under production, such as Bayan Obo, and those that are at various development stages. Kiviniemi ferrodiorite-hosted Sc deposit is also included (Halkoaho et al., 2020; Hokka and Halkoaho, 2016). According to Wang et al. (2021), magmatic rocks with average Sc contents of more than 60 ppm can be regarded as potential Sc deposits.

**Table 1. Main features of selected Sc deposits (adapted under CC BY 4.0 license from Paper I © 2021 Authors).**

| Deposit (country) | Resource Est. t @ Grade | Main Host Minerals for Sc | Deposit Type | References |
|---|---|---|---|---|
| Bayan Obo (China) | 140 000 t; 200 ppm Sc in tailings | Aegirine | Carbonatite | Williams-Jones and Vasyukova (2018) |
| Kovdor (Russia) | 420 t @ 509 ppm Sc | Baddeleyite | Carbonatite | Kalashnikov et al. (2016) |
| Tomtor (Russia | 100 Mt @ 390 ppm Sc | Xenotime (-Y) | Carbonatite (weathered) | Lapin et al. (2016), Williams-Jones and Vasyukova (2018) |
| Nyngan (Australia) | 16.8 Mt @ 235 ppm Sc | Adsorbed species on ferric oxyhydroxide in limonite and saprolite | Lateritic | Rangott et al. (2016) |
| Syerston (Australia) | 21.7 Mt @ 429 ppm Sc | Adsorbed species on goethite, hematite | Lateritic | Williams-Jones and Vasyukova (2018), Chassé et al. (2017) |
| Crater Lake (Canada) | Ind. 7.3 Mt @184 ppm Sc; inf. 13.2 Mt @ 172 ppm Sc | Hedenbergite | Ferrosyenite | (Imperial Mining Group Ltd., 2022) |
| Kiviniemi (Finland) | 13.4 Mt @ 163 ppm Sc | Hedenbergite, amphibole | Ferrodiorite | Hokka and Halkoaho (2016), Halkoaho et al. (2020) |

## 2.2 Overview of scandium production and main applications

As mentioned earlier, the current estimated global Sc production is only 15 to 25 tpa, with China dominating the production from the tailings of the Bayan Obo REE-Nb-Fe mine (Chassé et al., 2017; Eilu, 2017; U.S.Geological Survey, 2022; Williams-Jones & Vasyukova, 2018). In addition to the Bayan Obo tailings, Sc is usually produced as a by-product of beneficiation of Ni, Al, Ti, REE, U and Zr ores. As reported by the U.S. Geological Survey (2022), the prices of Sc have declined from 4.6 $/g in 2017 to an estimated 2.2 $/g in 2021 for $Sc_2O_3$ with 99.99% purity,

whereas the prices for metal (ingot) have increased from 132 $/g to 137 $/g during the same time span. As a reference, Y prices were 3–5 $/kg for 99.99% purity $Y_2O_3$ and 35–38 $/kg for Y metal. Furthermore, gold prices increased between 2017 and 2021 from 1261 $/troy ounce to an estimated 1800 $/troy ounce, equivalent to 41–58 $/g. The absence of a steady, long-term producer in addition to the extremely high prices has limited the commercial applications of Sc (Wang et al., 2011). New sources could provide the foundation for a more stable market and help to increase the use of Sc in high-technology applications. However, the occurrence of Sc as a trace element in mineral lattices inevitably reflects as the complexities in recovery flowsheets, depending on the quality and quantity of other elements involved.

Considering REE production in a wider perspective, after the traditional beneficiation of REE minerals, hydrometallurgy is most commonly used to extract individual elements, the other methods being electrometallurgy or pyrometallurgy (UNCTAD, 2014). Depending on the mineralogy of the REE-containing phases and the characteristics of gangue minerals, hydrometallurgical extraction may involve acidic or alkaline routes. According to Haque et al. (2014), the acidic route dominates at least 90% of extraction methods. Depending strongly on the mineralogy, roasting of the rare earth ore at 400–500°C in concentrated sulfuric acid can be used to remove fluoride and $CO_2$ and produce water-soluble phases (Haque et al., 2014). In addition to ore pretreatment, current hydrometallurgical processes include leaching, solvent extraction, precipitation, and calcination (Wang et al., 2011). The purified bulk product is often a solid oxide, carbonate, or chloride with a very low content of impurities, which is then further processed into desired end-products (Goode, 2019). The recovery of REE at Bayan Obo, currently the main producer of Sc, is conducted using low- and high-intensity magnetic separation, followed by flotation (Bisaka et al., 2017). Bayan Obo tailings, which contain 200 ppm Sc on average, are used for Sc recovery, employing roasting typically with sodium hydroxide, and subsequent leaching protocols (Williams-Jones & Vasyukova, 2018; Zhou et al., 2017).

Bauxite residues, or so-called red mud (RM), which is the main waste product of the Bayer process, with annual production rates approximated ~150 Mt (Khanna et al., 2022), have been extensively studied in recent decades as possible secondary resources of Sc (Li et al., 2018; Liu & Li, 2015). Bauxite residues generally contain 40–100 ppm Sc, although higher concentrations have also been reported for this highly alkaline, hazardous material (Akcil et al., 2018; Binnemans et al., 2015). In the hydrometallurgical processing of bauxite residues, the nonselective mobilization of Fe and Ti may deteriorate the purification and precipitation of

suitable Sc products (Alkan et al., 2017; Borra et al., 2015; Yagmurlu et al., 2018; Zhou et al., 2018). According to Yagmurlu et al. (2019), sustainable recovery of Sc from RM with selective iron recovery may be accomplished by combining pyrometallurgical and hydrometallurgical processes. Anawati and Azimi (2022) have also studied integrated carbothermic smelting—acid baking—water leaching process for bauxite residues. Furthermore, Li et al. (2014; 2018) conducted experiments with reductive roasting pretreatment of bauxite residue, in which hematite and goethite were reduced to metallic iron, followed by magnetic separation. Moreover, the PyEarth process has been developed by Mintek to recover REEs from iron-rich REE-bearing carbonatite ores of complex mineralogy in Southern Africa (Bisaka et al., 2017). The difficulties related to REE minerals with a particle size of less than 20 microns, disseminated in a matrix of iron oxide, are overcome in the PyEarth process by pyrometallurgical pretreatment to produce a Fe-Mn by-product and an REO-enriched slag for processing via hydrometallurgical methods (Bisaka et al., 2017).

Despite its excellent elemental properties, light-weight nature, and good alloying potential (Riva et al., 2016), production and usage of Sc in a larger scale have been hindered due to the challenges faced during its extraction and complexities in flowsheets. Scandium is currently mainly used in solid oxide fuel cells (SOFC's), in which it acts as a stabilizing agent for the solid electrolyte (Blengini et al., 2020; Zakaria & Kamarudin, 2021). It is estimated that Bloom Energy represents 80% of the world's annual consumption of Sc in SOFCs, and the consumption is expected to increase over the next decade (Minor Metals Trade Association, 2022).

Furthermore, Sc is known as the most effective microalloying element to contribute to the strength and weldability of Al–Sc alloys (Ahmad, 2003; Dorin et al., 2018; Lathabai & Lloyd, 2002). Adding alloying elements to an aluminum melt can be done either by adding pure elements or by adding the elements in the form of master alloys. Although adding pure Sc to the melt is technologically feasible, metallic Sc is excessively expensive (Royset, 2007). Chemical compounds, such as $ScF_3$, $ScCl_3$ and $Sc_2O_3$, can be transformed into Al–Sc master alloys by reducing reactions without a very complicated and costly process for producing pure metallic Sc; the most widespread master Al alloy contains 2 wt% Sc (Milman, 2006). Small additions of Sc (0.2–0.3 wt%) to Al create dispersed particles of intermetallic $Al_3Sc$ coherently bound with the Al matrix. The presence of these particles and the decreased grain size in cast metal increase its strength and plasticity characteristics (Dorin et al., 2018; Milman, 2006). As stated by Riva et al. (2016), Al–Mg–Sc

alloys may reduce the weight of an aerospace construction by up to 15–30% in comparison with common Al and Ti alloys, with the benefit of ensuring better mechanical and thermal characteristics in addition to better chemical stability. Al–Mg–Sc alloys with the trademark Scalmalloy® have been specifically designed for laser beam manufacturing (LBM) and aerospace structural applications (Begoc et al., 2019).

Furthermore, Sc alloys have been successfully implemented as hydrogen storage materials, in high-entropy alloys (HEAs) and in bulk metallic glasses, resulting in a new materials with lower density and higher hardness (Riva et al., 2016). Other Sc applications include mercury vapor high-intensity lights and activator ions in TV or computer monitors. In comparison to Y, Sc has much better electrical conductivity and superb heat-treating (and strengthening) dopant properties (Duyvesteyn & Putnam, 2014). In most applications, Sc has been used as a small-amount dopant, which hinders the possibility of recycling.

According to a recent summary published by the Minor Metals Trade Association (2022), Sc can be used in numerous large-volume applications, given sufficient supplies to meet the potential demand. In addition to the current main Sc suppliers from China and Russia, Sumitomo Metal Mining has built and commissioned an Sc recovery circuit at Taganito Bay nickel high-pressure acid leach (HPAL) plant in the Philippines, which recovers scandium oxalate ($Sc_2(C_2O_4)_3 \cdot xH_2O$) for processing into oxide (~7–8 tpa). Several operating and development projects utilizing HPAL technology to recover and separate Ni and Co in laterite deposits, are currently underway, many of which are generally able to recover Sc. Emerging projects, particularly in Australia, such as Nyngan and Syerston (currently known as Sunrise) (Table 1), are designing Sc recovery into their circuits alongside Ni and Co, with the potential output of Sc ranging from 50 to 100 tpa or even more.

With respect to titanium production, Chinese integrated titanium producer Lomon Billions has established a 20–30 tpa $Sc_2O_3$ facility with the potential to increase to 50 tpa in its titanium plants using the sulfate process (Minor Metals Trade Association, 2022). Furthermore, Rio Tinto has recently commenced Sc recovery from titanium dioxide by-products in its Sorel Tracy plant in Québec, Canada, which can supply 3 tpa of $Sc_2O_3$, with plans to produce Al–Sc master alloy (Rio Tinto, 2022). In addition, the recently commenced ScaVanger program (2021–2024) in the EU aims at recovering Sc through hydrometallurgical successive Sc, Nb, and V extraction from titanium acid waste solutions (EIT Raw Materials, 2022). ScaVanger focuses on chlorine-rich solutions from $TiO_2$ production mainly from

high grade $TiO_2$ feedstock (natural rutile, synthetic rutile, and upgraded titania slag), targeting the production of 21 tpa of $Sc_2O_3$. Recoverable resources are contained in liquid acid waste (60-140 mg/L of Sc, Yagmurlu et al., 2021). The residual metal-rich solutions are currently neutralized, dewatered, and mainly landfilled at high cost as filter cakes; some are also sold to chemical industries without any valorization of Sc, V, and Nb.

The only other currently known primary resource of Sc similar to the Kiviniemi deposit is the Crater Lake ferrosyenitic deposit in Canada (Table 1). The Crater Lake project is developed by Imperial Mining Group Ltd., which has reported indicated resources of 7.3 million t grading 184 g/t Sc and inferred resources of 13.2 million t with 172 g/t Sc for the Northern Lobe of the TG Scandium Zone (Imperial Mining Group Ltd., 2022). In addition to Sc, determinations of magnet rare earth oxides (Nd, Pr, Dy, Tb) have been made for both resource categories. Using a net smelter return (NSR) cut-off value of $CAN 110.80/t, the value of the mineralization was determined to be in the range of $CAN 386-413/t. With respect to beneficiation processes, Imperial Mining has reported results of LIMS and wet high-intensity magnetic separation (WHIMS) for two samples with differing mineralogy, producing mineral concentrates that yielded Sc recoveries of 78% and 88% in addition to total rare earth element (TREE) recoveries of 56% and 69%. They also reported dense media separation (DMS), yielding recoveries of 90.6% for Sc and 89.2% for TREE in the mineral concentrate. Optimization of the process parameters and the development of hydrometallurgical flowsheets for the Crater Lake project are currently underway. Hydrometallurgical processing is based on a two-stage extraction method with high-pressure caustic leaching (HPC), followed by hydrochloric acid leaching of the HPC residue, with reported recoveries of Sc to pregnant leach solution (PLS) of 87% and 84% for the two samples studied (Imperial Mining Group Ltd., 2022).

# 3 Kiviniemi intrusion

The Kiviniemi mafic intrusion (1857 ± 2 Ma) locates in the municipality of Rautalampi, approximately 70 km southwest of the city of Kuopio (Figures 3A,B) (Halkoaho et al., 2020; Hokka & Halkoaho, 2016). As stated by Halkoaho et al., (2020) it occurs near the eastern margin of the Paleoproterozoic Central Finland Granitoid Complex (CFGC) and is associated spatially and temporally with post-kinematic Fe-Ti-P-enriched Svecofennian orogenic mafic magmatism. The main relatively homogeneous ferrodioritic unit has a surface extension of ~2.5 hectares with an additional small satellite body. During drilling programs between 2008 and 2010 altogether nine holes were drilled at Kiviniemi. Medium- to coarse-grained garnet-bearing fayalite ferrodiorite bodies, enriched in Fe and Sc, are surrounded by transitional ferrodiorites and pyroxene ferromonzodiorites (Figure 3A). The country rock is porphyritic granite. As stated by Halkoaho et al. (2020) ferrodiorite and the surrounding granite (1860 ± 7 Ma) can be considered coeval within analytical error.

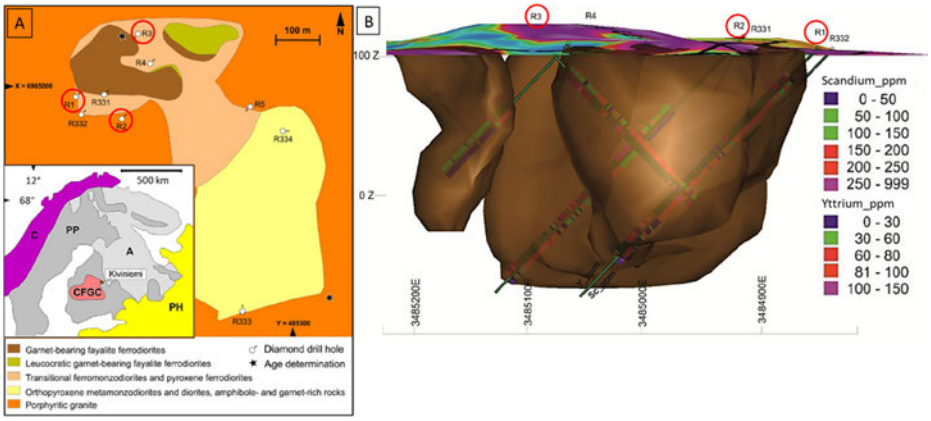


**Fig. 3. (A) Geological map of the Kiviniemi intrusion with the location and direction of the drill holes. The drill cores included in this study are indicated with red circles. (B) Fayalite ferrodiorite blocks of the Kiviniemi intrusion, the view is from the north (reprinted under CC BY 4.0 license from Paper I © 2021 Authors).**

An average Sc grade of 163 g/t with 1726 g/t Zr and 81 g/t Y have been reported for mineral resource of 13.4 Mt, which represents a preliminary estimate calculated with the inverse distance method (Hokka and Halkoaho, 2016). Mineral paragenesis is broadly similar for all ferrodiorites and leucoferrodiorites at

Kiviniemi; main minerals include (ferro)hedenbergitic clinopyroxene, almandine garnet, fayalitic olivine ($Fo_{1–4}$), amphibole (ferropargasite and ferroedenite), and plagioclase (average An ca. mol-40%) with grain sizes ranging typically between 100 and 2000 μm (Korhonen et al., 2011). According to Halkoaho et al. (2020) amphibole ($Sc_2O_3$ 103–2088 ppm, $n$ = 27), clinopyroxene (ferro)hedenbergite ($Sc_2O_3$ 818–1736 ppm, $n$ = 29) and fluorapatite ($Sc_2O_3$ 1062 and 1133 ppm, $n$ = 2) are the main carriers of Sc. Ilmenite, fluorapatite, zircon, magnetite, biotite, pyrite, pyrrhotite, quartz, clinoferrosilite and microcline are accessory minerals, of which ilmenite is the most common, occurring as inclusions, exsolution lamellae, and skeletal aggregates with magnetite, hematite, pyrite, and pyrrhotite. Strong recrystallization and corona formation overprint primary magmatic features; however, some relict cumulate textures have been preserved. Sporadic large potassic feldspar grains occur as xenocrysts from the surrounding granite (Halkoaho et al., 2020).

As stated by Halkoaho et al. (2020), the major element geochemical composition of the intrusion, coupled with its close association with the surrounding granite indicate that it belongs to the post-kinematic Paleoproterozoic magmatic stage of the Svecofennian orogen (ca. 2.0–1.77 Ga). However, the exceptionally high content of Sc in ferrodiorites (50–281 ppm, n = 42) deviates from the compositions of other Svecofennian mafic intrusions of the CFGC area. The Kiviniemi mafic body is geochemically metaluminous and tholeiitic and is significantly enriched in iron relative to magnesium. The main deposit ferrodiorites ($SiO_2$ 35.3–50.6 wt%, 44.8 ± 3.4 wt% on average, $n$ = 31) have $FeO_{tot}$ contents of 11.7–33 wt% (23.1 ± 3.7 wt% on average) and magnesium number (Mg#) of 5.0–10.9 (7.5 ± 1.55 on average). In addition to Sc, contents of Zr (275–5600 ppm), Y (58-189 ppm), Hf (7-115 ppm), and Ba (160-3586 ppm) are also elevated, whereas compatible element contents are comparatively low. The origin of the Sc enrichment at Kiviniemi is most probably magmatic, with Sc partitioning into ferromagnesian silicates and fluorapatite when these phases were stabilized. As discussed in Halkoaho et al. (2020), due to crystallization of the F- and P-bearing phases—fluorapatite at Kiviniemi—the activity of F and P ligands decreased in the magma (Gramaccioli et al., 2000; Shchekina & Gramenitskii, 2008), which may have resulted in a compatible behavior of Sc with respect to Fe–Mg silicates (Halkoaho et al., 2020).

# 4 Theoretical foundation

## 4.1 Magnetic separation

An overview of the general characteristics of minerals relevant to the Kiviniemi deposit, including density and mass magnetic susceptibility values (Mass $\chi$, $10^{-8}m^3/kg$), is provided in Table 2. The values of mass magnetic susceptibility are from the study of Hunt et al. (1995), unless stated otherwise, and refer to values measured in weak fields at room temperature. Large variations in the mass susceptibility values of minerals are due to the variability in the mineral chemical composition, the presence of inclusions, and different measuring techniques (Svoboda, 2004). The chemical composition of the minerals is the main controlling factor for their mass susceptibility values, with not only Fe but also Mn and Cu contents exerting the main effects on the extraction efficiency of paramagnetic minerals (Leißner et al., 2016; Rosenblum & Brownfield, 2000).

**Table 2. General characteristics of minerals relevant to Kiviniemi ferrodiorite as based on literature.**

| Mineral | Chemical Formula | Density g/cm$^3$ | Mass $\chi$ $10^{-8}m^3/kg$ |
|---|---|---|---|
| Apatite | $Ca_5(PO_4)_3(F,OH,Cl)$ | 3.20 | From −12.6 to −0.33* |
| Calcite | $CaCO_3$ | 2.71 | From −0.3 to −1.4 |
| Potassic feldspar | $KAlSi_3O_8$ | 2.56 | From −0.49 to −0.67 |
| Plagioclase | $NaAlSi_3O_8$-$CaAl_2Si_2O_8$ | 2.62 | −4.52* |
| Quartz | $SiO_2$ | 2.65 | From −0.5 to −0.6 |
| Zircon | $ZrSiO_4$ | 4.70 | From −0.73 to 164.60* |
| Amphibole | $NaCa_2(Fe_4Al)Si_6Al_2O_{22}(OH)_2$ | 3.44 | 6.5–380*** |
| Biotite | $KFe_3AlSi_3O_{10}(OH)_2$ | 3.17 | 52–98 |
| Chlorite | $(Fe,Mg)_5Al(Si_3Al)O_{10}(OH)_8$ | 3.20 | 10–35.2* |
| Clinopyroxene | $CaFeSi_2O_6$ | 3.55 | 8–80* |
| Fayalite | $Fe_2SiO_4$ | 4.39 | 130 |
| Garnet | $Fe_3Al_2(SiO_4)_3$ | 4.32 | 39.5–155.8* |
| Ilmenite | $FeTiO_3$ | 4.72 | 46–80,000 |
| Magnetite | $Fe_3O_4$ | 5.20 | 20,000–110,000 |
| Pyrite | $FeS_2$ | 5.02 | 1–100** |
| Pyrrhotite | $Fe_{(1-x)}S$ | 4.62 | 10–30,000 |

*Data from Nordman and Kuusisto, (1994); **magnetic property may change from diamagnetic to paramagnetic; ***susceptibility data for hornblende

The chemical and physical properties of Sc-bearing silicates, the bulk mineralogy of the deposit, and the textural features provide the main criteria for selecting appropriate beneficiation procedures. Regarding the concentration criterion (*CC*) and the practicality of gravity concentration—other than DMS—for the Kiviniemi Sc-bearing minerals, the density differences are considered inadequate for successful amphibole and pyroxene separation from gangue minerals. According to the criterion provided by Taggart (in Dunne et al., 2019) concentration criterion is calculated

$$CC = (D_h - D_f)/(D_l - D_f) \quad (1)$$

in which $D_h$ = density of the heavy particles (g/cm$^3$), $D_l$ = density of the light particles (g/cm$^3$) and $D_f$ = density of the fluid (water 1.0 g/cm$^3$). Clinopyroxene and amphibole as the main Sc-bearing minerals in the Kiviniemi deposit have an average density of 3.5 g/cm$^3$, whereas the dominant gangue minerals, plagioclase, and potassic feldspar, have an average density of 2.6 g/cm$^3$. Therefore, the CC value of 1.6 falls into the range of very difficult separation (Dunne et al., 2019).

Given the paramagnetic characteristics of the Kiviniemi Sc-containing minerals (Table 2) and the proposed processing scheme (Figure 1), wet magnetic separation with SLon pulsating high-gradient magnetic separator (PHGMS) was chosen for the preconcentration. According to information obtained from the earlier beneficiation study (Korhonen et al., 2011), 72% Sc recovery with 346 ppm Sc grade was achieved by applying low intensity and high gradient magnetic separation. This information together with general characteristics of paramagnetic mineral separation with SLon (Chen & Xiong, 2015), and the nature of the Kiviniemi feed material (Table 2) were used to select experimental parameters for SLon. Separation to magnetic and non-magnetic fractions with SLon occurs via a combination of magnetic force, pulsating fluid and gravity (Dobbins et al., 2009; Metso Outotec, 2022). The filamentary matrix is constructed of rods orientated perpendicular to the applied magnetic field at equal distances, optimizing the magnetic force and minimizing the risk of entrapment of diamagnetic particles. The separation performance is enhanced by pulsation in the separation zone, which agitates the slurry and keeps all particles in a dispersed state, simultaneously minimizing the entrapment of diamagnetic minerals. This mechanism also ensures maximum particle accumulation on the rod matrix. In addition to minimized particle entrapment, another benefit of SLon is its applicability to separate fine fractions (Chen & Xiong, 2015; Dobbins et al., 2009).

## 4.2 High-temperature reduction

### *4.2.1 Thermodynamic basis*

Differences in the thermodynamic properties of oxides form the basis for selective reduction of ferrous oxide in a system containing $Sc_2O_3$. The high affinity of Sc to oxygen provides the theoretical foundation for the reduction and separation of metallic products from $Sc_2O_3$-containing slag (Gupta & Krishnamurthy, 2005; Faris et al., 2017). Figure 4 shows molar Gibbs standard free energies of formation as a function of temperature, known as the Ellingham diagram, with selected oxides that are relevant to the Kiviniemi ferrodiorite concentrate.

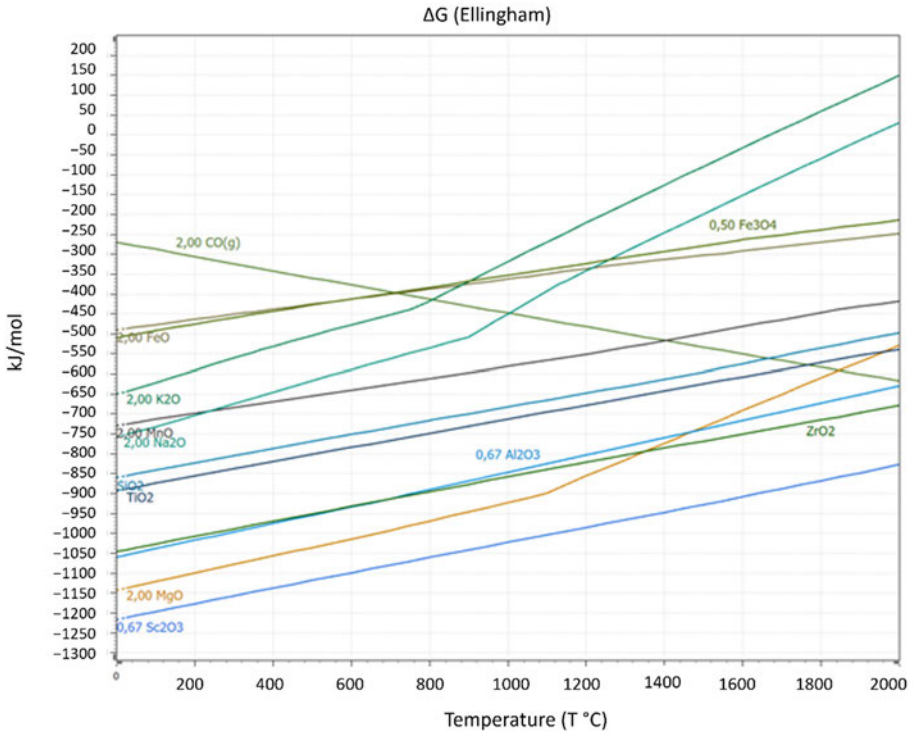


**Fig. 4. Ellingham diagram for the pure oxides relevant to the Kiviniemi concentrate. Gibbs free energy data were obtained from HSC Chemistry.**

With increasing temperature, the stability of oxides decreases, making them easier to be reduced. Scandium oxide is in the lowermost part of the diagram, indicating

the high stability of $Sc_2O_3$ in comparison to the other oxides, particularly ferrous and ferric oxides present in the Kiviniemi concentrate. The free energies of formation of the compounds involved determine the feasibility of the reduction process; however, the practicability is determined by other properties of the material, such as melting characteristics, vapor pressure, density and viscosity, in addition to chemical reactivity and alloying behavior of the various reactants and products (Gupta & Krishnamurthy, 2005). Although the direction of the expected reactions in the system is provided by the standard free energy data, it does not indicate the reaction rate (kinetics), which should be investigated by experimental methods, such as thermogravimetric analysis (TGA).

### *4.2.2 Thermogravimetric analysis*

The kinetics of the reaction can be determined via measuring changes in the sample mass with temperature through TGA method, applicable particularly for clearly defined process in the TG curve, e.g., stoichiometric dehydration of a definite hydrate (Brown, 2004; Saadatkhah et al., 2020). The extent of conversion is determined experimentally as a fraction of the total mass loss (Vyazovkin et al., 2011). The kinetic parameters of discrete solid-state reactions can be determined with several analytical methods, unlike the analysis of complex processes (Perejón et al., 2011). Furthermore, with heterogeneous materials, overlapping and interacting phenomena originating from various reactions within and from various types of crystal structures may occur. Table 3 presents high-temperature characteristics for minerals relevant to Kiviniemi concentrate based on the literature.

Various mineral reactions include dehydration, dehydroxylation, thermal dissociation, and gas–solid reduction reactions at lower experimental temperatures, in addition to which at higher experimental temperatures melting, slag formation, gas–liquid, and solid–liquid reduction reactions are included (Foldvari, 2011; Saadatkhah et al., 2020). Furthermore, diffusion and heat transfer account for the whole scenario in addition to chemical reactions at reactant/product interfaces. Moreover, during dynamic experiments, heat transfer from the furnace to the outer regions of the sample and into the sample, self-cooling or self-heating of the sample during reactions, removal of evolved gaseous product, and the influence of these products on the rates of reactions—all contribute to the reaction processes (Brown, 2004).

Since the physical properties measured by the thermogravimetric method are not specific to species and, therefore, usually cannot be linked directly to specific reactions of molecules, the value of conversion reflects the progress of the overall transformation of the starting material to the products (Vyazovkin et al., 2011). The overall transformation, particularly in this study with heterogeneous starting material, involves many reactions, each of which has a specific extent of conversion. However, some of the potential reduction reactions contributing to the observed mass loss are discussed in Paper II.

**Table 3. General high-temperature characteristics of minerals relevant to Kiviniemi ferrodiorite as based on literature (adapted under CC BY 4.0 license from Paper II © 2022 Authors).**

| Mineral | Chemical Formula | High-T Characteristics | References |
|---|---|---|---|
| Apatite | $Ca_5(PO_4)_3(F,OH,Cl)$ | Fluorapatite melting point at 1660°C | Kaia et al. (2012) |
| Calcite | $CaCO_3$ | Decomposes at 897°C to CaO and $CO_2$ | Kracek (1963) |
| Potassic feldspar | $KAlSi_3O_8$ | Incongruent melting 1150°C; eutectic with $SiO_2$ at 990°C | Kracek (1963) |
| Plagioclase | $NaAlSi_3O_8$-$CaAl_2Si_2O_8$ | Albite melting point at 1118°C; anorthite melting point at 1550°C | Kracek (1963) |
| Quartz | $SiO_2$ | Quartz melting point (metastable) 1470°C | Kracek (1963) |
| Zircon | $ZrSiO_4$ | Decomposes to oxides below liquidus, 1540°C | Kracek (1963) |
| Amphibole | $NaCa_2(Fe_4Al)Si_6Al_2O_{22}(OH)_2$ | Dehydroxylation begins at >500°C; decomposes to pyroxene, spinel, olivine and feldspars; beginning of melting at 1100°C | Brett et al. (1970), Hodgson et al. (1965) |
| Biotite | $KFe_3AlSi_3O_{10}(OH)_2$ | Dehydroxylation 600-1000°C | Brett et al. (1970) |
| Chlorite | $(Fe,Mg)_5Al(Si_3Al)O_{10}(OH)_8$ | Dehydroxylation begins at ~450°C (in air) | Zhan and Guggenheim (1995) |
| Clinopyroxene | $CaFeSi_2O_6$ | Stable below 965°C; decomposes into $CaSiO_3$ solid solution; melting relations are ternary, mixtures 0–72% $FeSiO_3$ behave in binary manner. | Kracek (1963) |
| Fayalite | $Fe_2SiO_4$ | Melting point at 1205°C | Kracek (1963) |
| Garnet | $Fe_3Al_2(SiO_4)_3$ | Decomposes at 900°C | Kracek (1963) |
| Ilmenite | $FeTiO_3$ | Melting point at 1450°C | Kracek (1963) |
| Magnetite | $Fe_3O_4$ | Melting point at 1597°C; reduction reactions already at low temperature | Kracek (1963) Yang et al. (2014) |
| Pyrite | $FeS_2$ | Reduction begins at 500°C | Schwab and Philinis (1947) |

### 4.2.3 Calculation with FactSage

FactSage 7.2 was used to test whether theoretical equilibrium calculation provide consistent results with our experimental data (Paper II). Accessibility to high quality thermodynamic database covering the given system of interest and the correctness of the algorithm that minimizes the total Gibbs energy of a system with a given set of constraints are two important preconditions for accurate thermodynamic calculations (Jung & Van Ende, 2020). As multiple databases can be selected for calculations, FToxid, FSStel and FactPS were used. FToxid database for slags, glasses, minerals, ceramics, refractories, etc. contains consistently assessed and critically evaluated thermodynamic data for stoichiometric oxides and oxide solid solutions formed by 23 elements (Jung & Van Ende, 2020; Penttilä, 2014). The crystal structures of more than 80 solid solutions, such as spinel, olivine, melilite, pyroxenes, perovskite, wollastonite, etc. are modeled in the framework of the compound energy formalism (CEF) (Jung & Van Ende, 2020). As stated by Penttilä (2014) the core system ($Al_2O_3$-CaO-FeO-$Fe_2O_3$-MgO-MnO-$SiO_2$) has been fully optimized from 25°C to above liquidus temperatures for all compositions and oxygen partial pressures.

Figure 5 displays the result of equilibrium calculation on the stability of crystalline phases, formation of solid and liquid metal, and liquid slag formation as a function of temperature using the average concentrate composition from all composite Kivniemi samples (100 g concentrate, 100 g CO and 5 g C in a temperature range of 500–1500°C). Fayalite, hedenbergite, and potassic feldspar in addition to the plagioclase end-members albite and anorthite are the main crystalline phases at equilibrium at temperature range 500–800°C. Hydrous minerals were excluded in this calculation, resulting in high amounts of fayalite and feldspars. The presence of minor crystalline phases suggested by calculation is also shown in the figure 5, although they were not present in the concentrate. The calculations indicate that metallic iron occur at ~820 °C due to reduction of fayalite and hedenbergite. Along the increasing temperature and progression of reduction of ferrous silicates, intermediate crystalline phases can be formed, which is similar to results reported in other experimental studies (Massieon et al., 1992; Massieon et al., 1993; Xiaoyang, 1996). According to this calculation, hedenbergite is stable until ~820°C, after which it decomposes into crystalline diopside $CaMgSi_2O_6$ and wollastonite $CaSiO_3$ along with the reduction of the ferrous oxide component to metallic iron.

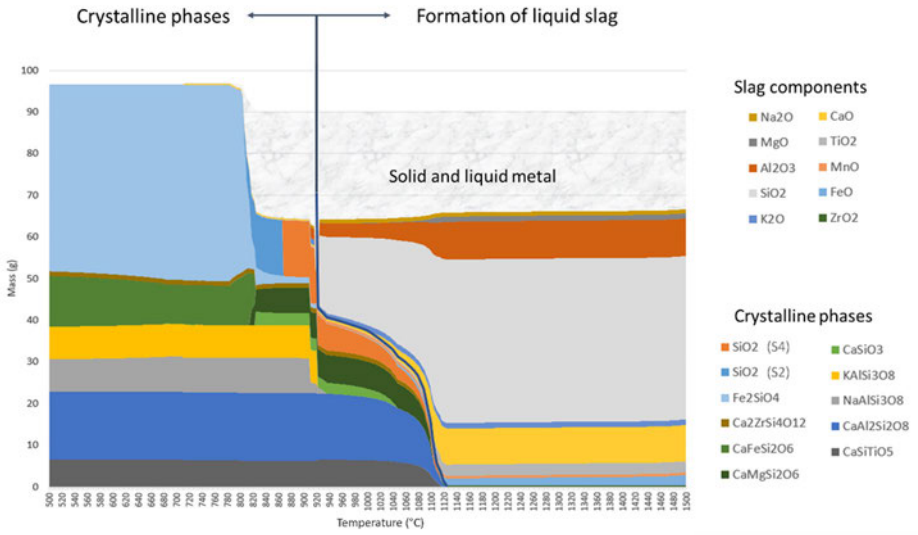


**Fig. 5. FactSage 7.2 equilibrium calculation for average concentrate composition, showing the stability of crystalline phases and the formation of liquid slag and combined solid and liquid metal as a function of temperature (reprinted under CC BY 4.0 license from Paper II © 2022 Authors).**

### *4.2.4 Modifying slag characteristics*

One of the most important properties of metallurgical melts, which directly affect the kinetic conditions of the processes, is viscosity (Kekkonen et al., 2012; Kondratiev et al., 2002; Seetharaman et al., 2005). Viscosity is related to the internal structure of the oxide melt. It is very sensitive to changes in temperature, slag composition, and oxygen partial pressure (Kekkonen et al., 2012; Verein Deustcher Eisenhüttenleute, 1981). The transfer of mass and heat, the solubility of slag formers and modifiers, and the separation of metal and slag are improved with low viscosities. $SiO_2$, as a network former, forms strong, highly covalent bonds, leading to high liquid viscosities. Network-transforming alkali and alkali earth oxides, such as $Na_2O$, $K_2O$, MgO, CaO, and other divalent oxides, such as MnO and FeO, decrease viscosity by breaking this network (Kondratiev et al., 2002; Mills et al., 2013; Seetharaman, 2005; Seetharaman et al., 2005). Depending on the composition of the slag system, amphoteric oxides such as $Al_2O_3$ may act either as a network former or transformer (Mills et al., 2013; Park et al., 2004). As the slags contain both covalent and ionic bonds, and the extent of polymerization varies with

the metal oxide and flux contents in the slag, the quality and quantity of ions and electrostatic interactions in addition to the temperature have significant impact on slag viscosity (Kekkonen et al., 2012; Mills et al., 2013).

CaO or $CaF_2$ additions are commonly used in metallurgical operations to lower the viscosity of slag (Kato & Minowa, 1969; Seetharaman et al., 2005; Wu et al., 2011). Slag composition with a suitable liquidus temperature is essential in industrial practices in addition to appropriate viscosity. The ternary $Al_2O_3$–CaO–$SiO_2$ phase diagram presented in Figure 6 exhibits the target area with lower liquidus temperatures, as indicated in the close-up, which was used to design the type and quantity of doping. To calculate and plot the compositions with FactSage version 7.2 and its FToxid database on the phase diagram, only the main oxide components of our slag system were considered.

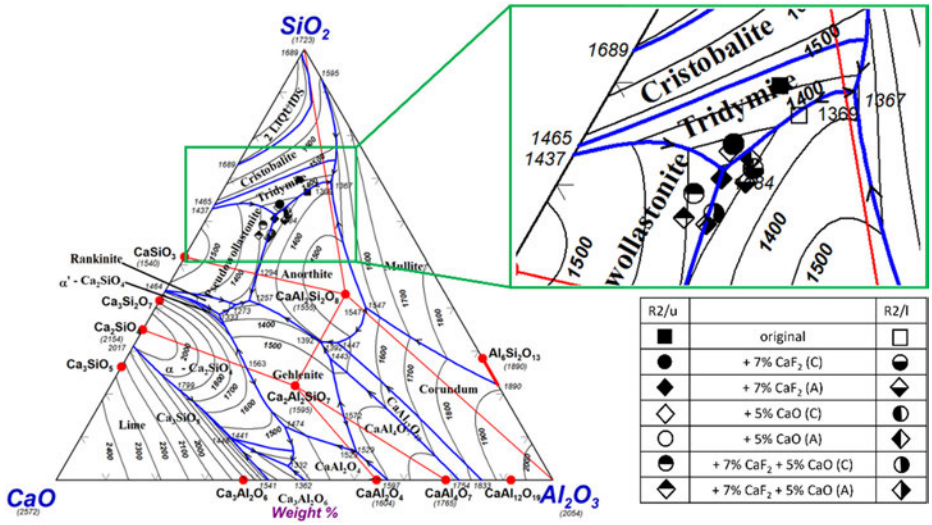


**Fig. 6. Ternary phase diagram with the target liquidus temperature area displayed in the close-up view. Original and modified slag compositions from R2/u and R2/l concentrates were computed and plotted with FactSage version 7.2 and its FToxid database. C was calculated from ICP-OES data and A was calculated from EPMA analysis data (reprinted under CC BY 4.0 license from Paper III © 2022 Authors).**

## 4.3 Hydrometallurgical extraction

Leaching, solvent extraction, and precipitation are common hydrometallurgical processes for Sc extraction from various types of sources. According to Wang et al.

(2011) precipitation of insoluble Sc compounds from Sc-containing solutions has been mentioned as the easiest method to recover Sc; however, problems may arise from nonselective mobilization of Fe and Ti. These tend to deteriorate the purification and precipitation of suitable Sc products due to similar physicochemical properties (Alkan et al., 2017; Borra et al., 2015; Yagmurlu et al., 2018; Zhou et al., 2018). Mineral acids are considered the best leaching agents for scandium recovery from various sources, but ionic liquids and organic acids have also been explored (Botelho Junior et al., 2021).

Silica gel formation is one of the most common problems at lower temperatures in the hydrometallurgical processing of silica-containing resources, such as bauxite residues, which have $SiO_2$ contents in the range of 3.0–30.0 wt% (Alkan et al., 2018; Binnemans et al., 2015; Wang et al., 2011). In acidic conditions (pH <7), soluble silica is found as monomer orthosilicic acid, $Si(OH)_4$ (Queneau and Berthold, 1986), which may connect to each other through Si-O-Si branches to form polysilicic acid and eventually colloids. Gelation occurs when these colloids connect with each other becoming unfilterable with liquid entrapped inside (Alkan et al., 2018). Temperature, pH level, the degree of supersaturation, the presence of seed particles, and salinity control the gelation rate (Queneau and Berthold, 1986). Other disadvantages in the direct sulfuric acid leaching of bauxite residues include a low selectivity toward Fe, Ti and Sc, and the co-precipitation of Sc in an acidic iron sulfate mineral, rhomboclase, formed by dissolution of Fe oxide and subsequent reprecipitation as sulfate (Alkan et al., 2018).

Implementing hydrogen peroxide creates oxidative conditions in leaching, which has been reported to lead to the precipitation of dissolved Si as quartz without silica gel formation (Alkan et al., 2018). Furthermore, the formation of a titanium peroxosulfate complex yielding a high-Ti leaching efficiency and decreasing the amount of Sc-entrapping rhomboclase precipitation have been mentioned. As an example, leaching efficiencies of Sc from bauxite residues increased from 27% at room temperature to 68% at 90 °C after 30 min of the leaching and S/L of 1:10 in $H_2O_2$-assisted $H_2SO_4$ leaching (Alkan et al., 2018).

Another possible method to avoid silica gel formation is dry digestion, which consists of the addition of a concentrated acid to solid materials with subsequent water leaching (Alkan et al., 2019; Rivera et al., 2018; Voßenkaul et al., 2017). Dry digestion is very similar to acid baking, which is conducted at higher temperatures (200–400°C) (Alkan et al., 2019; Kim and Azimi, 2020). With dry digestion, Sc leaching efficiencies from acidic, RM residue-derived slags with a high content of amorphous material have been reported to reach 70% (Alkan et al., 2019). In the

studies of Kim and Azimi (2020), acid baking and Sc leaching from crystalline blast furnace slag reached a maximum extraction efficiency of 89.4%. Furthermore, according to Rivera et al. (2019), high-pressure acid leaching (HPAL) may also provide an opportunity for Sc extraction (up to 90%) while using $H_2SO_4$ at 150°C. Moreover, oxidative pressure acid leaching has been shown to be an effective method for metal extraction, particularly for slags containing crystalline phases (Baghalha et al., 2007; Li et al., 2009; Perederiy, 2011; Perederiy and Papangelakis, 2017). However, also for amorphous slag Sc extraction yields of up to 85 wt% with HPAL have been reported (Rivera et al. 2019).

With respect to Sc in aqueous solution, the properties of $Sc^{3+}$(aq) are suggested to be closer to those of $Al^{3+}$ (ionic radius 54 pm) than to $Y^{3+}$ (93 pm) or the lanthanide ions due to smaller ionic radius (in octahedral coordination 75 pm, Shannon, 1976). Sc(III) functions as a hard metal ion (Pearson, 1963), although fluoride and hydroxide complexes are unusually strong in relation to its charge/radius ratio (Schrödle et al., 2008). The distribution of Sc–hydroxide complexes as a function of pH and temperature are shown in Figure 7 (adapted from Wood and Samson, 2006), according to which at 25°C, the $Sc^{3+}$ ion predominates at pH <4, whereas at 300°C, unhydrolyzed $Sc^{3+}$ is not predicted to be present in significant quantities (Wood and Samson, 2006).

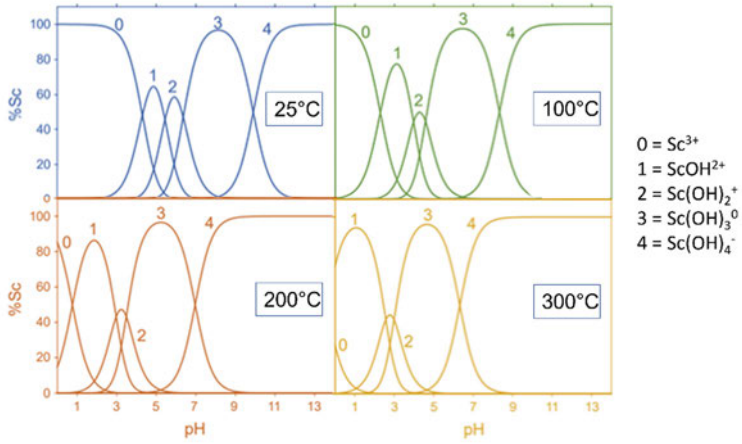


**Fig. 7. Distribution of $Sc^{3+}$ hydroxide complexes as a function of pH at 25°C, 100°C, 200°C and 300°C at saturated water vapor pressure (adapted from Wood and Samson, [2006], with permission from Elsevier).**

HSC Chemistry 10 software was utilized to establish the Eh-pH diagram for Sc-S aqueous system at 50°C, 75°C and 100°C (Figure 8). Scandium exists as $Sc^{3+}$ in our experimental conditions according to this diagram; $Sc^{3+}$ stability area is slightly decreased toward the lower acidity region with increasing temperature.

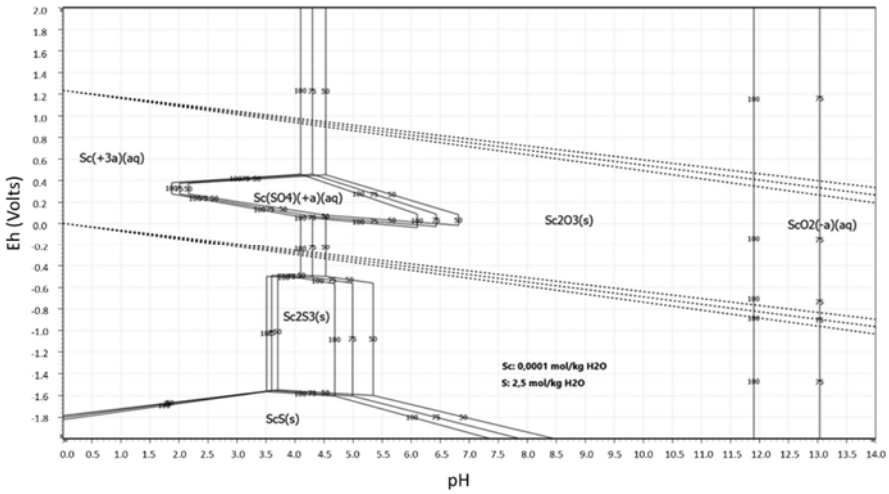


**Fig. 8. Eh-pH diagram for the Sc-S aqueous system at 50°C, 75°C and 100°C (reprinted under CC BY 4.0 license from Paper IV © 2022 Authors).**

# 5 Materials and methods

## 5.1 Samples

GTK delivered samples of Kiviniemi Sc-enriched rocks to this study as crushed drill core material (<4 mm). Three adjacent or proximal drill core samples (Figure 9) were included from a total of four drill core intervals (a total of 12 samples), with their selection based on the availability of suitable samples, as well as the dimensions and the average estimated Sc grade of the deposit. These were processed into four composite samples to provide sufficient material for laboratory-scale experiments. Composite samples were coded as and referred to in the following way: R1 composite sample from drill core R1; R2/upper (R2/u) and R2/lower (R2/l) composite samples from drill core R2; and R3 composite sample from drill core R3. Most of the Sc at Kiviniemi is contained in medium- to coarse-grained garnet-bearing fayalite ferrodiorite, which was the most prominent rock type in these samples.

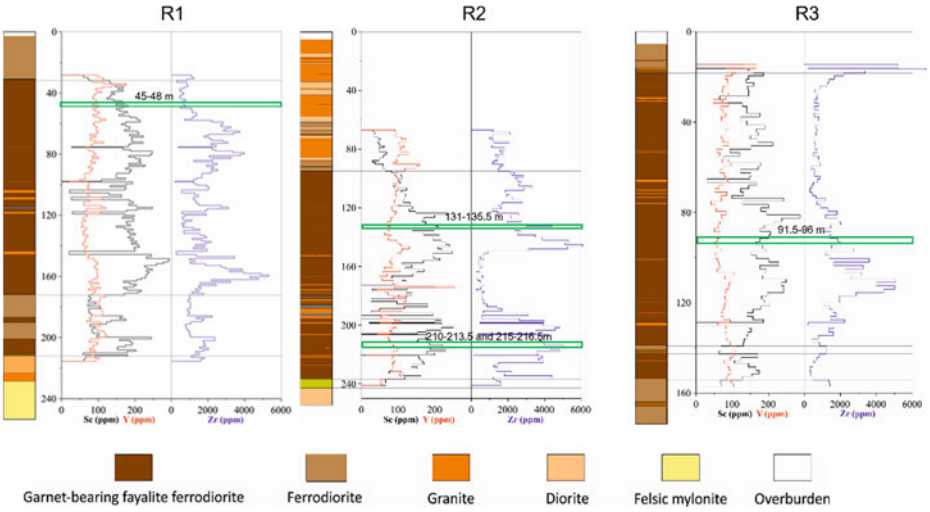


**Fig. 9. Lithological columns and variations of Sc, Y and Zr contents in drill cores R1, R2 and R3, respectively, with the locations of the samples of this study indicated with green rectangles. Note the different scale (in meters) for each column (reprinted under CC BY 4.0 license from Paper I © 2021 Authors).**

As described in Paper I, the samples were split with a sample splitter, half of which was processed for magnetic separation experiments. The split samples were first

dry sieved with a Retsch sieve shaker (10 min with an amplitude of 1.5 mm). Combined coarser fractions (>125 µm) were ground with a Wedag rod mill (H × D = 30.5 cm × 15 cm) with a constant rotation frequency of 100 rpm. Wet grinding with 11 stainless steel rods (7 pcs, 30 cm × 1.9 cm; and 4 pcs, 30 cm × 1.4 cm) with a total mass of 7.05 kg and a solid percentage of 60% were used. Samples were ground as approximately 1 kg aliquots for 1 h, after which they were dried, combined, and mixed thoroughly with fine fractions. The target $P_{80}$ close to or less than 90 µm was considered appropriate at the beginning of the study. This was considered suitable for magnetic separation experiments with also a possibility to conduct flotation experiments that were considered an option at the beginning of the study.

## 5.2 Material characterization and analysis methods

ICP–OES was chosen as the quantitative bulk elemental analysis method, and all analyses of solid samples were conducted by Eurofins Labtium in Kuopio and Eurofins Ahma in Oulu, Finland. Prior to sending them for analysis, dry samples were pulverized to 100% -90 µm with a tungsten carbide mill at Oulu Mining School. As described in Papers I and III, for ICP–OES analysis, the prepared pulp samples (0.2 g) were fused with anhydrous sodium peroxide in zirconium crucibles by heating them in an electric furnace at 700°C for one hour. The resulting melt was then dissolved in hydrochloric acid, and the final solution diluted with water prior to the instrumental analysis. 27 elements with a Thermo Electron ICAP 6500 Duo instrument are analyzed according to routine method. Detection limits with quality control details are provided as electronic supplementary data in Paper I.

For modal mineralogy, INCAMineral software (Version 5.05) and a Zeiss ULTRA Plus instrument (Field Emission Scanning Electron Microscope [FESEM]) at the Centre for Material Analysis (CMA), University of Oulu, were used on polished vertical blocks of all concentrates and tailings (Ø 25 mm). To minimize the effects of the touching particles, graphite was added to the samples. The following instrumental parameters were applied: acceleration voltage of 15 kV, beam current of 2.3 nA, and working distance of 8.3 mm. For each sample, a minimum of 10000 detected features were set and post-processing conducted with GrainAlyzer software.

As described in Paper IV, slag residues obtained after leaching experiments were characterized with a JEOL JSM-7900F FESEM equipped with an Oxford Instruments Ultim Max 65 energy dispersive (EDS) detector and Aztec Mineral

software at the CMA. A small amount of residue powder was placed onto carbon scotch tape, after which the samples were coated with carbon. Secondary electron images with X-ray mapping and point analyses were conducted with an accelerating voltage of 15 kV, 5 nA probe current, and a working distance of 10 mm.

For mineral, slag, metal, and leach residue compositional analysis, electron probe microanalyzer (EPMA) JEOL JXA-8530FPlus was used at the CMA. Analyses were carried out on carbon-coated polished blocks (Ø 25 and 40 mm). An accelerating voltage of 15 kV, a beam current of 15 nA and a beam diameter 1-10 μm were used. The peak and background counting times were set at 10 s and 5 s, respectively, for all components. Furthermore, for scandium, peak and background counting times of 30 s and 15 s were also tested and applied. Matrix correction with the atomic number—absorption—fluorescence (ZAF) method was applied. Data on detection limits and the standards used are provided as electronic supplementary data in Papers I, II and Paper IV.

A Rigaku SmartLab 9 kW X-ray diffraction (XRD) apparatus with a Co anode was used with 40 kV and 135 mA settings to monitor the presence of crystalline phases at selected temperatures after high-temperature experiments and to characterize the slags produced as well as the solid residues after leaching experiments. The speed of acquisition was 4°/min with 0.02°/step and 2θ range of 10–130°. PDXL2 software and the PDF-4 2022 database were used for data processing.

Particle size distributions for Kiviniemi drill core samples after comminution were determined with wet screening. Particle size distributions for slags continuing to leaching experiments were determined with Anton Paar particle size analyzer 1190 LD (laser diffraction) in liquid measurement mode with obscuration target values between 5% and 30%. Water was used as the carrier liquid without dispersing agents; satisfactory dispersion was obtained via ultrasound.

Carbon and sulfur analyses for slag samples were conducted with a LECO CS 200 Carbon and Sulfur Analyzer. Geostats Mining Industry Consultants Reference Material Manufacture and Sales Certified Reference Material GGC-07 (C = 0.56 wt%, S = 0.51 wt%) was used as a calibration standard. Analysis method C 0.5–S 0.5 with 40 s analysis time was applied. An iron chip accelerator + Lecocell Combustion accelerator was used as the blank sample. The accuracy of the results was 0.01% for C and 0.005% for S.

Agilent 5110 VDV ICP-OES instrument at the University of Oulu was used for determining Al, Ca, Fe, K, Mg, Mn, Na, Sc, Si and Ti in the 10-fold-diluted

solutions from leaching experiments. The analytical results are given as a mean value of five replicate measurements. Yttrium (wavelenght 371.029) was used as an internal standard to correct for sensitivity drift and matrix effects during the measurements. Quality control standards and blank samples were measured for quality assurance purposes. For each sample, 10-, 40-, and 200-fold dilutions with 2% nitric acid were made. The results for Al, Ca, and Ti were taken from the 200-fold diluted samples; the results for Mg and Na were taken from the 40-fold diluted samples; and the rest of the results were taken from the 10-fold diluted samples.

## 5.3 Magnetic separation

Magnetic separation experiments with LIMS WD(20) 111–15 and SLon 100 were carried out at the laboratories of the Metso Outotec Research Centre, Pori, Finland. In our study with SLon100, the effect of magnetic induction (0.3, 0.5, 0.7 and 1.0 T) and the frequency of pulsation (50, 150 and 250 rpm) were investigated (Paper I). Information from the earlier beneficiation study (Korhonen et al., 2011), characteristics of paramagnetic mineral separation with SLon (Chen and Xiong, 2015) and characteristics of the feed (Hunt et al., 1995; Nordman and Kuusisto, 1994) were used in selecting experimental parameters. SLon separations were conducted for ~200 g batches. The recovery ($R$) of Sc was calculated according to

$$R = \frac{Cc}{Cc+Tt} * 100 \quad (2)$$

in which $Cc$ refers to the concentrate mass and Sc grade, respectively, and $Tt$ refers to the tailings.

## 5.4 High-temperature experiments

Schematics of the thermogravimetric (TG) furnace used at the Process Metallurgy Research Unit, University of Oulu, is provided in Paper II. The furnace has $Al_2O_3$ chamber, which allows experimental temperatures up to 1500°C. Mettler Toledo AG 204 balance (accuracy ± 0.1 mg) was used to follow the changes in the sample mass along with a set temperature program. Parameters were controlled with an in-house developed software and data were recorded with approximately 5 s intervals. The temperature was controlled with Eurotherm 3508 and measured with an S-type thermocouple. The gas flow (2 L/min) was controlled with a Brooks 5850S mass flow controller. The heating rate was 5 °/min, with the target temperatures and

isotherms at the set target temperature following the experimental protocols presented in Papers II and III. At the cooling stage, the flow of $N_2$ was 5 L/min. Fractional extent of reactions—or degree of conversion ($\alpha$)—was calculated (Brown, 2004; Cai et al., 2018) according to

$$\alpha = (m_0 - m)/(m_0 - m_f) \quad (3)$$

in which $m_0$ = initial mass, $m$ = mass at each stage of the experiment, and $m_f$ = mass at the end of the experiment. The derivate conversion was calculated using the degree of conversion to provide more details about the conversion rate. Smoothing was applied using averages of 10 measurements to decrease the noise in derivative plots. The following formula was applied to calculate the derivative conversion curves by means of the central difference

$$(d\alpha/dX)i = 1/2(\alpha_i - \alpha_{i-1})/(X_i - X_{i-1}) + 1/2(\alpha_{i+1} - \alpha_i)/(X_{i+1} - X_i) \quad (4)$$

where $\alpha$i and ($d\alpha/dX$)i are the conversion and derivative conversion of the $i$-th point, respectively, and $X$ can be either temperature ($T$) or time ($t$).

In addition to the similar experimental procedure used in the first part of the pyrometallurgical study (Paper II), quickly cooled samples at selected temperatures were included in the second stage to investigate the progression of mineral reduction reactions at various temperatures (Paper III). For these experiments, the gas composition was changed to 95% Ar and 5% $H_2$. The sample was raised to the upper, cooler part of the furnace after reaching the desired temperature in the TG furnace, to cool with a $N_2$ gas flow, and taken out of the furnace after a few minutes of cooling.

## 5.5 Slag production for leaching experiments

For leaching experiments, synthetic slag with a selected composition was prepared from pure oxides with details provided in Paper IV. Chemicals were mixed and melted at 1700°C in a platinum crucible, after which molten slag was quenched on a water-cooled copper plate to ensure its completely amorphous structure. The produced slag was first crushed and ground to the size of less than 125 µm, after which further grinding to $D_{90}$ ~30 µm was conducted using Herzog tungsten carbide vibratory disc mill. In addition to synthetic slag, authentic Kiviniemi concentrates were processed by reducing the FeO component prior leaching experiments in an Entech high-temperature gradient furnace as 100 g batches. The details of Kiviniemi slag production are given in more detail in Paper IV. After reduction and

cooling, the samples were first removed from the graphite crucible, and the large metal accumulations were removed from the bottom. The slag was cut into four pieces and crushed with Geopyörä breakage test (Bueno et al., 2021). After crushing, the slag samples were ground with Herzog tungsten carbide vibratory disc mill to the target particle size of $D_{90}$ ~30 µm. The final magnetic separation with a hand magnet (NdFeB) was conducted to remove residual metal inclusions from the slag as much as possible.

## 5.6 Leaching experiments

A summary of three the $H_2SO_4$-based methods to test slag samples is presented in Figure 10. Only a few dry digestion experiments were conducted in an open decanter for 10 g samples, but due to very low extraction efficiencies, the experiments were directed toward $H_2O_2$-assisted acid leaching. The main part of the leaching experiments, atmospheric $H_2O_2$-$H_2SO_4$ leaching, was performed in a 0.25-L reactor immersed in a silicon oil bath and using 5.00 ± 0.005 grams of Sc slags per experiment. The reactor was closed using a reflux condenser to prevent volatilization during leaching. Selected process variables (acid concentration, temperature, time, S/L ratio) for the leaching were investigated first to optimize Sc yield with synthetic slag, after which Kiviniemi R1 and R3 slags were tested with selected parameters. In all our experiments, the agitation speed was maintained at 375 rpm using a magnetic stirrer. The total leaching time was 90 min. Pressurized leaching experiments were performed in a Hastelloy C22 stainless-steel reactor (Parr, Moline, IL, USA) equipped with a cylindrical HASTELLOY®C-267 alloy autoclave (300 mL). The details of leaching experiments and their procedures are given in Paper IV.

The leaching efficiency ($\eta i$) for metal extraction can be calculated in a variety of ways. In this study, equation 5 was applied for all leaching experiments (Zhou et al., 2018)

$$\eta i = \frac{ciV}{mxi} * 100\% \quad (5)$$

in which $m$ is the mass of the slag, $c_i$ is the metal concentration in the leaching solution, $V$ is the volume of leaching solution, and $x_i$ is the mass fraction of the metal element in the slag. For comparison, solid residues from few experiments were also analyzed with ICP-OES to calculate the yield using the following equation

$$X = (1 - (\frac{Cr}{Co})) * 100\% \quad (6)$$

where $C_r$ and $C_o$ are the scandium content in the residue and in the original slag, respectively.

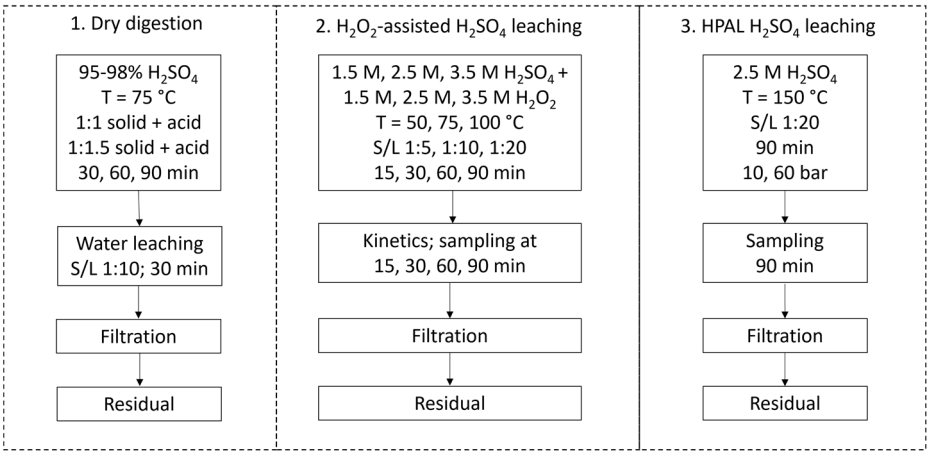


**Fig. 10. $H_2SO_4$-based methods which were tested with synthetic and Kiviniemi slags.**

## 5.7 Summary

A summary of the research and characterization methods applied with corresponding samples studied in relation to each research stage are presented in Table 4.

**Table 4. Research and characterization methods used with corresponding samples studied.**

| Research stage | Experiments/materials | Sample | FESEM | EPMA | ICP-OES* | ICP-OES** | XRD | TGA | PSD | LECO |
|---|---|---|---|---|---|---|---|---|---|---|
| 1. Magnetic separation | LIMS1, LIMS 2, LIMS 3 MAGS | R1, R2/u, R2/l, R3 | X | X | X | | | | | |
| | SLon 0.5T+150rpm MAGS + NMAGS | R2/l | X | | X | | | | | |
| | SLon 0.5T+50rpm MAGS + NMAGS | R1, R2/u, R2/l, R3 | X | X | X | | | | | |
| | SLon 0.5T+250rpm MAGS + NMAGS | R2/l | X | | X | | | | | |
| | SLon 0.3T+150rpm MAGS + NMAGS | R2/l | X | | X | | | | | |
| | SLon 1.0T+150rpm MAGS + NMAGS | R1, R2/u, R2/l, R3 | X | X | X | | | | | |
| | SLon rougher-cleaner 1 + 2 | R2/l | X | | X | | | | | |
| 2. Pyrometallurgy | 1350, 1400, 1450, 1500°C | R2/l | | X | | | | X | | |
| | 1100+1350°C, 1100+1450°C | R2/l | | X | | | | X | | |
| | 1450°C + CaO | R2/l | | X | | | | X | | |
| | 1450°C + $CaF_2$ | R2/l | | X | | | | X | | |
| | 1450°C + CaO + $CaF_2$ | R2/l | | X | | | | X | | |
| | 1500°C + CaO | R1, R2/u, R3 | | X | | | | X | | |
| | 1500°C + $CaF_2$ | R1, R2/u, R3 | | X | | | | X | | |
| | 1500°C + CaO + $CaF_2$ | R1, R2/u, R3 | | X | | | | X | | |
| | 950, 1050, 1150, 1250, 1350°C + CaO | R3 | | X | | | X | X | | |
| | 1550°C gradient furnace | R1, R3 | | X | X | | X | | X | X |
| 3. Hydrometallurgy | Dry digestion 75°C | Synthetic | | | | X | | | | |
| | Reflux cond.; T 50, 75, 100°C | Synthetic, R1, R3 | | | | X | X | | | |
| | Reflux cond. 100°C; molarity | Synthetic, R1, R3 | X | X | X | X | X | | | |
| | Reflux cond. 100°C; S/L | Synthetic, R1, R3 | X | X | X | X | X | | | |
| | HPAL 150°C | Synthetic, R3 | | | X | X | X | | | |

*ICP-OES analyses at Eurofins Ahma from solid samples; **ICP-OES analyses at the University of Oulu from liquids

# 6 Results and discussion

A summary of the materials and the main findings and articles produced during the progression of this study are presented in Figure 11. The main results of each stage are briefly presented in the following chapters.

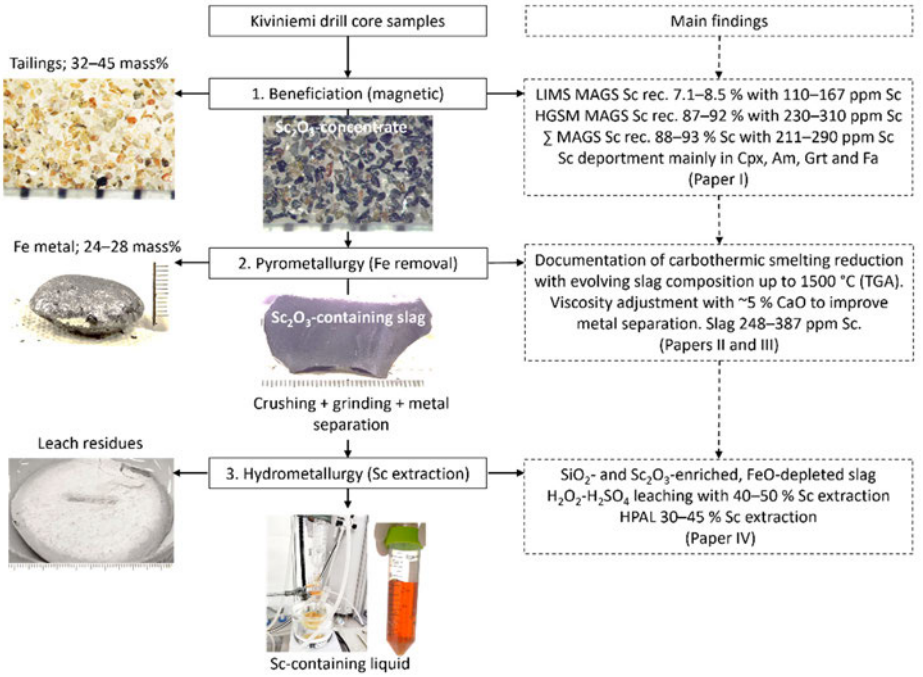


**Fig. 11. Research process with main findings and produced materials.**

## 6.1 Magnetic separation (Paper I)

Paper I deals with the process mineralogical characteristics of Kiviniemi ferrodiorite samples included in this study and the applicability of LIMS + PHGMS to separate diamagnetic, alkali-bearing gangue minerals from ferro- and paramagnetic minerals, which include the main Sc carriers, ferrous clinopyroxene and amphibole. The target $P_{80}$ for samples was close to or less than 90 µm, which was achieved with wet grinding for 60 min. Sample R1 from the upper part of the intrusion contains almost 50% < 32 µm after comminution, which is attributed to the more extensive alteration compared to the samples from the lower parts of the

intrusion, as based on microscopic observations. The three magnetic LIMS fractions (Mags1, Mags2, and Mags3) removed, in total, 9.5, 9.0, 9.6 and 8.0 mass% of the feed for R1, R2/u, R2/l and R3 composite samples, respectively (Figure 12). LIMS efficiently removes particles containing ferromagnetic minerals, magnetite and monoclinic pyrrhotite, into the magnetic fractions, with the total iron oxide plus pyrrhotite recovery usually exceeding 70%. However, as magnetite and pyrrhotite both occur on grain boundaries, as inclusions and, particularly magnetite, in complex symplectitic mineral intergrowths and reaction rims, ternary occurrences account for most magnetite and pyrrhotite occurrences. Considering that the sum of feed ferromagnetic minerals varied only between 1.7 and 2.6 mass%, aforementioned textural features resulted in a relatively high mass% of LIMS concentrates in all the composite samples with a relatively high Sc content.

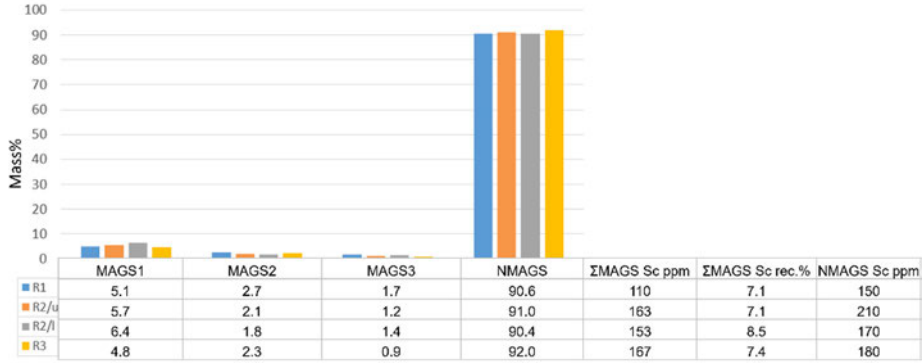


| | MAGS1 | MAGS2 | MAGS3 | NMAGS | ΣMAGS Sc ppm | ΣMAGS Sc rec.% | NMAGS Sc ppm |
|---|---|---|---|---|---|---|---|
| R1 | 5.1 | 2.7 | 1.7 | 90.6 | 110 | 7.1 | 150 |
| R2/u | 5.7 | 2.1 | 1.2 | 91.0 | 163 | 7.1 | 210 |
| R2/l | 6.4 | 1.8 | 1.4 | 90.4 | 153 | 8.5 | 170 |
| R3 | 4.8 | 2.3 | 0.9 | 92.0 | 167 | 7.4 | 180 |

**Fig. 12. LIMS magnetic and non-magnetic fractions from Kiviniemi composite samples (reprinted under CC BY 4.0 license from Paper I © 2021 Authors).**

Rougher separations were performed first on the R2/l composite sample using three different pulsation frequencies (50, 150 and 250 rpm) and applied magnetic inductions of 0.3, 0.5 and 1.0 T. Various pulsation frequencies were tested first with the magnetic induction of 0.5 T, after which the magnetic inductions 0.3 and 1.0 T were tested with selected pulsation frequency of 150 rpm. The effect of pulse frequency appears to be more significant with respect to recovery at the rougher stage than the applied magnetic induction strength. Furthermore, at a pulsation of 150 rpm, the highest applied magnetic induction appeared to provide the best results. Two sets of rougher-cleaner tests were also carried out for the R2/l composite sample with a pulse frequency of 150 rpm, varying the applied magnetic induction from 0.5 to 1.0 T and from 0.7 to 1.0 T. Regarding the cleaner stages, in

the first cleaner test the grade was only slightly improved to reach the value of 270 ppm with significant decrease in recovery to 78%. In the second cleaner test, the grade was not improved, with only slight improvement in the recovery. Therefore, two sets of experimental parameters (1 = 50 rpm pulsation with 0.5 T and 2 = 150 rpm pulsation with 1.0 T) targeting high recoveries at the rougher stage were chosen to be also applied to the composite samples R1, R2/u and R3. An improvement in the quality was more obvious for R1 and R2/l concentrates with the 150 rpm pulsation and 1.0 T applied magnetic induction (Figure 13). With respect to magnetic separation, the commonly occurring iron-rich lamellae in clinopyroxene promotes magnetic separation, which is supported by negligible losses of clinopyroxene to tailings.

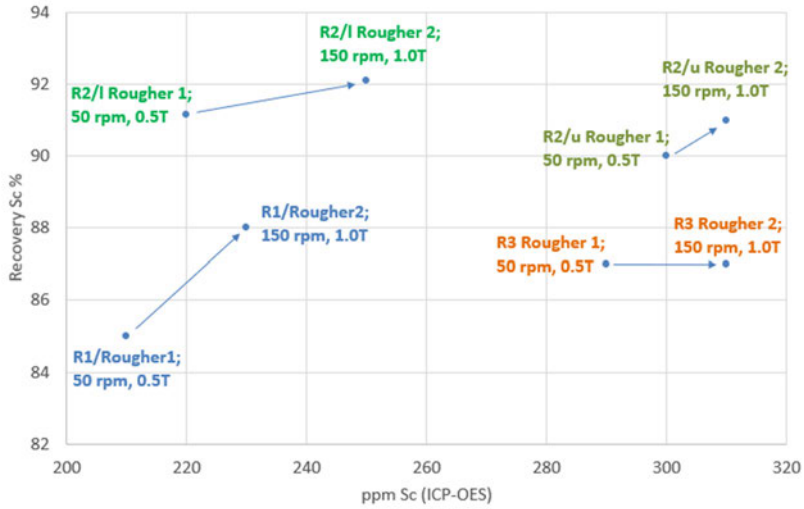


**Fig. 13. Effects of SLon rougher parameters (1 = 50 rpm pulsation with 0.5 T and 2 = 150 rpm pulsation with 1.0 T) on the Sc grade and recovery from all four composite samples.**

Based on the results of EPMA analysis, in addition to the main Sc carriers, clinopyroxene (130–1490 ppm, $n$ = 238) and amphibole (0–1420 ppm, $n$ = 188), $Sc_2O_3$ was detected mainly in garnet (0–260 ppm, $n$ = 39), fayalite (0–220 ppm, $n$ = 33) and zircon (0–300, $n$ = 15). Results above the detection limits (>100 ppm) were also occasionally observed for ilmenite, clinoferrosilite, plagioclase and potassic feldspar. Similar results were reported by Halkoaho et al. (2020), with the main carriers of Sc in the ferrodiorites being amphibole (103–2088 ppm $Sc_2O_3$, $n$ = 27) and clinopyroxene (818–1736 ppm, $n$ = 29). Apatite was also mentioned to

include Sc (1062 and 1133 ppm, $n = 2$), which contrasts with the analytical results of this study. Similarly to this study, Halkoaho et al. (2020) documented the following Sc-bearing phases: zircon (averaging 187 ppm $Sc_2O_3$), garnet (44–343 ppm, $n = 6$), clinoferrosilite (0–199 ppm, $n = 13$), and plagioclase (22–175 ppm, $n = 18$). $Sc_2O_3$ contents in both main carriers exhibit a wide variation in all composite samples, as presented in more detail in Paper I.

Both LIMS and SLon magnetic concentrates were combined to create the feed for pyrometallurgical experiments; modal mineralogy for R1, R2/u, R2/l and R3 samples produced with LIMS and SLon parameters 1.0 T and 150 rpm are illustrated in Figure 14.

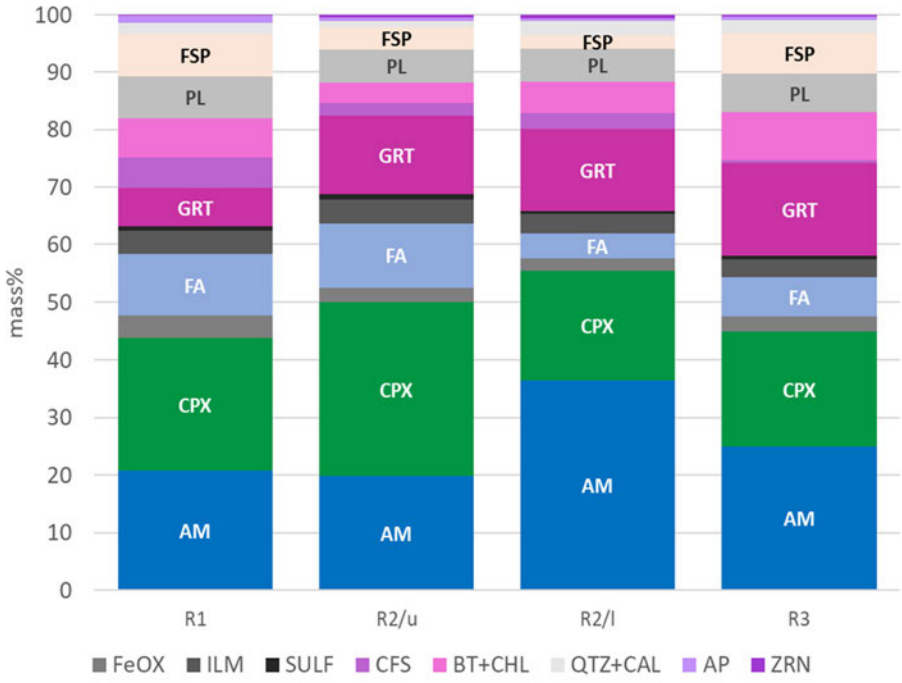


**Fig. 14. Modal mineralogy compositions of combined LIMS and SLon (1.0 T + 150 rpm) concentrates AM = amphibole; CPX = clinopyroxene; FeOX = magnetite; FA = fayalite; ILM = ilmenite; SULF = sulfides (both pyrrhotite and pyrite); GRT = garnet; CFS = clinoferrosilite; BT = biotite; CHL = chlorite; PL = plagioclase; FSP = potassic feldspar; QTZ = quartz; CAL = calcite; AP = apatite; ZRN = zircon (adapted under CC BY 4.0 license from Paper III © 2022 Authors).**

Deportment calculations were carried out using EPMA-based average contents together with modal mineralogy data (Figure 14), as discussed in more detail in Paper I. Variation in modal compositions of the samples as well as variation in the $Sc_2O_3$ contents of both main carriers reflect to the differences between the grades and the deportment between the concentrates. Figure 15 presents the results of normalized deportment calculation for main components (CaO, $SiO_2$, $Al_2O_3$ and FeO) and $Sc_2O_3$ in amphibole, clinopyroxene, fayalite and garnet in all the concentrates produced with LIMS and SLon using parameters 1.0 T and 150 rpm.


**Fig. 15. Deportment calculation of main components and $Sc_2O_3$ in amphibole (AM), clinopyroxene (CPX), fayalite (FA) and garnet (GRT) for the R1, R2/u, R2/l and R3 concentrates produced with LIMS and SLon (1.0 T + 150 rpm) (modified under CC BY 4.0 license from Paper III © 2022 Authors).**

As summarized in Paper I, process mineralogical research revealed variation in intrinsic properties of clinopyroxene and amphibole and indicated variation in the modal mineralogy of the composite samples. Furthermore, minor Sc deportment to other ferrous minerals, mainly fayalite and garnet, was detected. Revealing the causes for the observed variance of $Sc_2O_3$ in the main carriers would require a more specific study in this issue only, which is beyond the scope of this study. The composite samples included in this study from various parts of the main Sc-containing unit exhibited mutually similar behaviors in magnetic separations; highest Sc recoveries (87–92% with 230–310 ppm Sc) were achieved with SLon

experimental parameters of 150 rpm and 1.0 T. As stated in Paper I, maximizing both the recovery of $Sc_2O_3$ and $FeO_{tot}$ while decreasing those of $SiO_2$, $K_2O$ and $Na_2O$ by the removal of paramagnetic minerals into tailings (32–45 mass% in this study for combined LIMS + SLon concentrate) was considered beneficial for the proposed high-temperature reduction stage.

## 6.2 Reduction characteristics (Paper II)

In the first part of the pyrometallurgical studies (Paper II), the R2/l concentrate was used without any additions other than graphite to characterize the reduction up to temperatures of 1300°C, 1400°C, 1450°C and 1500°C. Although TG curves of complex materials, such as those represented by the Kiviniemi concentrate, are not directly interpretable or easy to fingerprint in terms of specific reduction reactions, some of the potential main reactions contributing to the measured mass loss were presented and discussed in Paper II.

The main reduction reactions are considered essentially similar to iron oxide reactions, although the progression of the FeO component reduction from the lattices of silicate minerals is more complex than iron oxide reduction reactions (Sarma et al., 1996; Yang et al., 2014; Yu et al., 2014), with kinetics hindered by the mass transfer phenomena within the silicate lattices at lower temperature ranges. Amphibole has the main effect on the reduction reactions and observed conversion rates due to the main deportment of FeO in the amphibole in R2/l concentrate. Reduction reactions for amphiboles containing divalent iron in their lattice occur at higher temperatures than for amphibole with trivalent iron (Brett et al., 1970). The main reduction stage for R2/l concentrate initiates from 950°C onwards with a sharp increase in the conversion rates between 1050°C and 1170°C and continues as the forming FeO-containing slag reacts with graphite with relatively high rates of conversion until ~1250°C. Based on EPMA analysis results, the smelting reduction of the iron oxide component in the liquid slag with graphite is completed at the highest temperature (1500°C). Although most of the metal forms large accumulates consisting of ferrite, $Fe_3C$ and $Fe_3P$ in addition to graphite, metal entrapment even at the highest temperature is prominent due to the very high viscosity of the slag.

In addition to the reduction of the FeO component, the reduction of silica in the slag by solid carbon and iron may occur at temperatures above 1400°C (Maroufi et al., 2016; Ray et al., 2018; Tangstad, 2013). According to Lee and Kolbeinsen (2021), the reduction of $SiO_2$ takes place only after the main FeO reduction in

ferromanganese and silicomanganese smelting processes, similarly to this study. Titanium and phosphorus oxides are minor oxide components with the main deportment in ilmenite and apatite, respectively. According to metal and slag analyses, the extent of $TiO_2$ reduction in our experiments was limited. Although Kennedy et al. (2017) have reported high temperatures (>1400°C) for apatite reduction via solid carbon and metallic iron, phosphorus eutectic was present in large metal accumulations in all the experiments of this study. As stated in Paper II, silica may help in breaking the phosphate bond, releasing free $P_2O_5$ gas, which may react with carbon via the Boudouard reaction or be directly reduced with carbon (Yang et al. 2014). Furthermore, the MnO component in liquid slag can be reduced with carbon, and a mechanism involving metallic iron has also been suggested (Safarian et al., 2009). A small amount of Mn in the metal accumulate was detected only in the experiment conducted up to the highest temperature.

As summarized in Paper II, the melting and formation of liquid slag promotes the segregation and accumulation of metal. However, the viscosity of the slag increases as the FeO component is reduced, hindering the diffusion of the remaining FeO and causing the entrapment of small metal inclusions in the slag, which is somewhat compensated by the increasing temperature. Promotion of the segregation of small metal droplets and separation of as much metal as possible through suitable modification of the slag composition was considered preferable prior to hydrometallurgical processing.

## 6.3 Modifying slag properties (Paper III)

Paper III focuses on the second stage of pyrometallurgical experiments, which were designed to complement the characterization of the reduction behavior of Kiviniemi ferrous Sc concentrates from three perspectives: (1) modifying the slag composition with $CaF_2$ and/or CaO to lower the viscosity of the slag and promote the reduction of the FeO component with enhanced separation of metallic iron, (2) comparing the reduction of a variety of concentrates from various parts of the Kiviniemi mafic intrusion with selected $CaF_2$ and/or CaO doping, and (3) describing in more detail the main features of the progression of reduction with CaO addition at selected temperature intervals (950°C, 1050°C, 1150°C, 1250°C, and 1350°C).

As discussed in Paper III, both additions alone (CaO and $CaF_2$) applied in the amounts to reach the target liquidus temperature area, as presented in the ternary $Al_2O_3$–CaO–$SiO_2$ phase diagram in Figure 6, exhibited a wider temperature range

for higher rates of conversion as compared to the combined and thus the highest amount of doping. This is due to enhanced slag-forming reactions and lower viscosity, which improve the kinetics of reduction reactions within narrower temperature intervals with the highest amount of doping. In addition to the complete reduction of FeO and $P_2O_5$, reduction of the MnO, $TiO_2$, $K_2O$, and $SiO_2$ components from slag occurred to some extent, particularly with $CaF_2$ additions. The surface characteristics of the slags with $CaF_2$ doping (Figure 16A,C) differ from the slags with CaO-only doping (Figure 16B); $CaF_2$ is known to be a surface-active constituent in slags (Nakamoto et al., 2007). The wetting behavior of slag without an FeO component at graphite–slag interfaces has been regarded as rather poor depending on the carbon-slag interfacial tension, slag and carbon surface tension, and the dynamic reactions occurring at the interface (Siddiqi et al., 1997), which is altered by $CaF_2$.

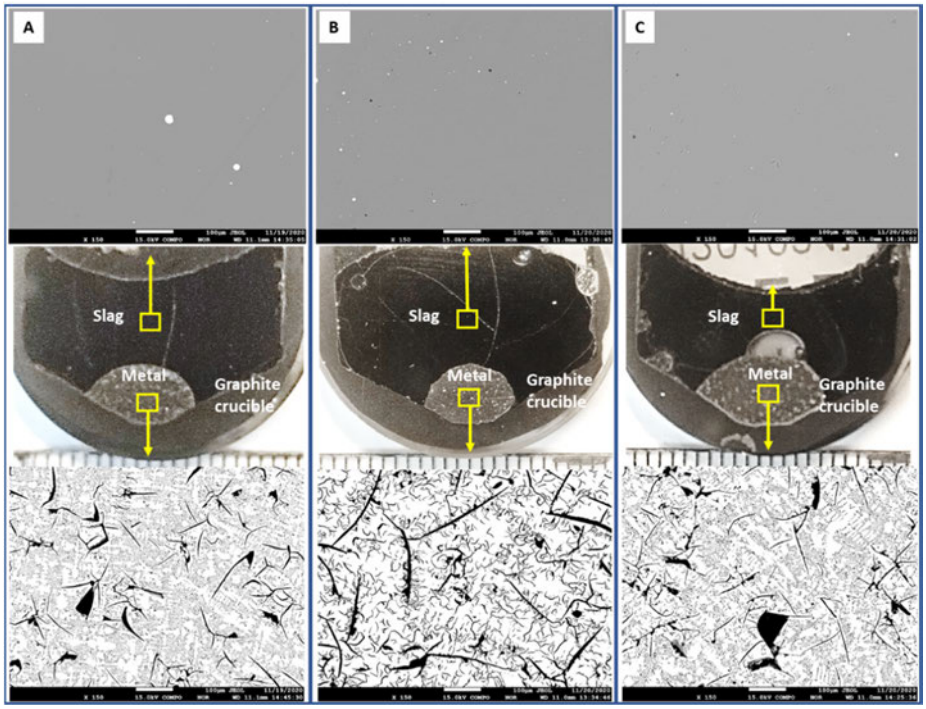


**Fig. 16. Back-scattered electron images of slag and metal after experiments with concentrate R3 conducted up to 1500°C with various dopants. (A) 7% $CaF_2$, (B) 5% CaO and (C) 7% $CaF_2$ + 5% CaO. White metal droplets occur in the slag (reprinted under CC BY 4.0 license from Paper III © 2022 Authors).**

Large graphite-bearing metal accumulations include similar phases as described in Paper II; eutectic steadite between Si-containing ferrite and flake graphite and/or interdendritic graphite segregations (Figure 16). Titanium carbide (TiC) was occasionally detected at the borders between ferrite and graphite. Graphite crystallization in cast gray iron is controlled by melt composition, temperature, and cooling rate (Radzikowska, 2017; Stefanescu et al., 2018); higher silicon content in the metal appeared to promote the tendency to form fine interdendritic graphite. As illustrated in Figure 16, metallic iron somewhat penetrated the graphite crucible, dissolving carbon into the metal and producing the aforementioned textures upon cooling. Furthermore, the gasification reactions at the Fe–C surface as proposed by Teasdale and Hayes (2005a; 2005b) produce CO as one of the reaction steps involved in the reduction of slag by solid carbon in the presence of liquid Fe–C; liquid Fe–C metal and gas-forming reactions from various slag components contribute to the reactions between liquid slags and carbon (White et al., 2017).

To reveal the main features of the progression of reduction, R3 concentrate with 5% CaO was reduced at selected temperatures (950°C, 1050°C, 1150°C, 1250°C, and 1350°C) as the final aspect of pyrometallurgical studies. This dopant would be preferable for slag modification due to environmental aspects and other harmful issues related to the usage of $CaF_2$ (Persson et al., 2007; Wang et al., 2006; Moreira et al., 2018). In these experiments, a mixture of Ar and $H_2$ was used to eliminate the possibility of a reversed Boudouard reaction. With respect to the baseline experiment conducted with Ar + $H_2$, the main stage of ferrous silicate reduction reactions peaked at ~1050°C, with similar final mass changes of 15.19 and 14.88% at 1500°C for 100% CO and 95% Ar + 5% $H_2$, respectively. The progression of the reduction processes at different temperatures is presented in Figure 17, which illustrates the derivative conversion curve of the baseline experiment with photographs and back-scattered electron images of the samples.

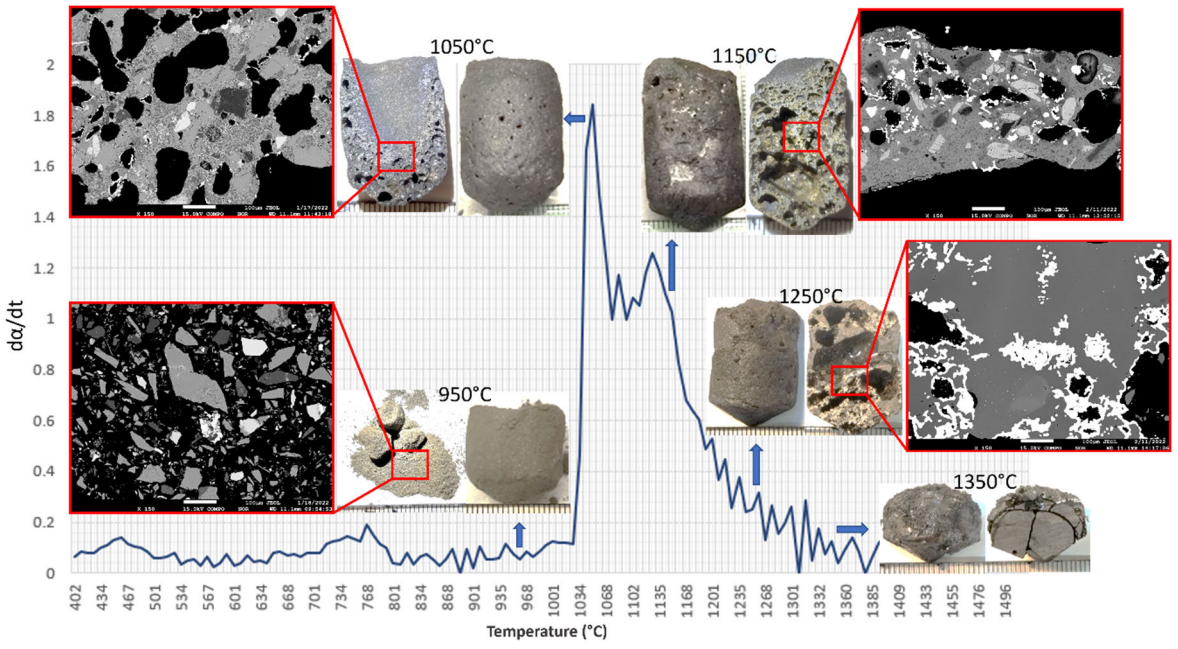


**Fig. 17. Photographs of samples at different temperatures (950°C, 1050°C, 1150°C, 1250°C, and 1350°C), plotted on the derivative conversion curve of the baseline experiment with 95% Ar + 5% $H_2$. The back-scattered electron images of the samples visualize the progression of mineral decompositions and slag and metallic iron formation (adapted under CC BY 4.0 license from Paper III © 2022 Authors).**

The changes at 950°C were very limited, with differences between clinopyroxene and amphibole reactions visualized in more detail in Figure 18. At this temperature, clinopyroxene appeared as an intact mineral with the original composition and structure, whereas the destruction of the original amphibole and the formation of new solid phases, including minuscule metallic iron particles within the relict of an amphibole crystal, had occurred due to dehydroxylation and reaction with the reducing gas. The XRD patterns in Figure 19 demonstrate the complexity of concentrate crystal structures at 950°C, with identifiable patterns for potassic feldspar, plagioclase, clinopyroxene, garnet, fayalite, ilmenite, and even amphibole, with relicts occasionally preserved within larger grains.

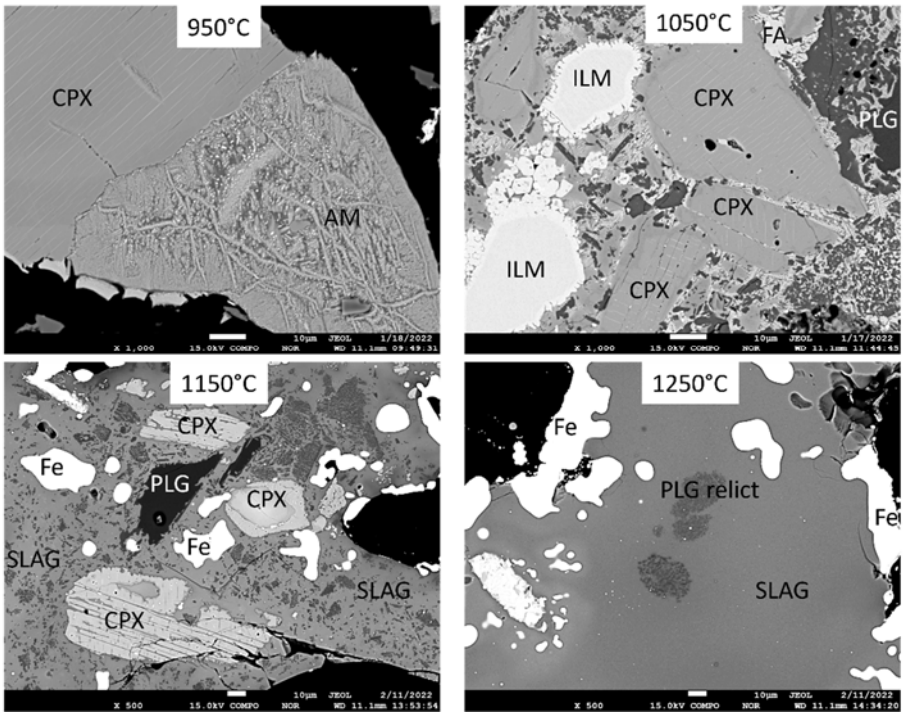


**Fig. 18. Back-scattered electron images of mineral reactions and progression of decomposition with formation of slag and metallic iron at 950°C, 1050°C, 1150°C, and 1250°C. Mineral abbreviations: CPX = clinopyroxene, AM = amphibole, ILM = ilmenite, FA = fayalite, PLG = plagioclase, Fe = metallic iron (reprinted under CC BY 4.0 license from Paper III © 2022 Authors).**

At 1050°C, the decomposition of amphibole and garnet dominate the formation of initial slag. Gas-forming reduction reactions created porosity around graphite particles, producing metal rims around the pores (Figure 17). Phases such as pyroxene, spinel, olivine, feldspars, and silica in addition to melt have been mentioned as decomposition products of various types of amphibole (Brett et al., 1970; Grapes, 2006). Furthermore, metallic iron, cristobalite, and hercynite, with fayalite as a secondary product have been detected under reducing conditions (>1000°C) after the decomposition of garnet (Aparicio et al., 2010). In R3 samples, the common decomposition products were very fine-grained mixtures of dark, lath-shaped crystals with a composition resembling that of plagioclase, and an FeO-rich phase (Figure 18). Clinopyroxene, ilmenite, potassic feldspar, and plagioclase were more persistent primary minerals at this temperature, which exhibited reaction rims, dissolution structures, and zoning, as illustrated in Figure 18. Clinopyroxene and plagioclase were identifiable in the XRD patterns in addition to metallic iron and graphite (Figure 19). The amount of metallic iron and slag increased along the progression of reduction reactions at 1150°C (Figure 17). Minor peaks were still identifiable for clinopyroxene and plagioclase in addition to metallic iron, which is the dominant phase in the XRD patterns (Figure 19).

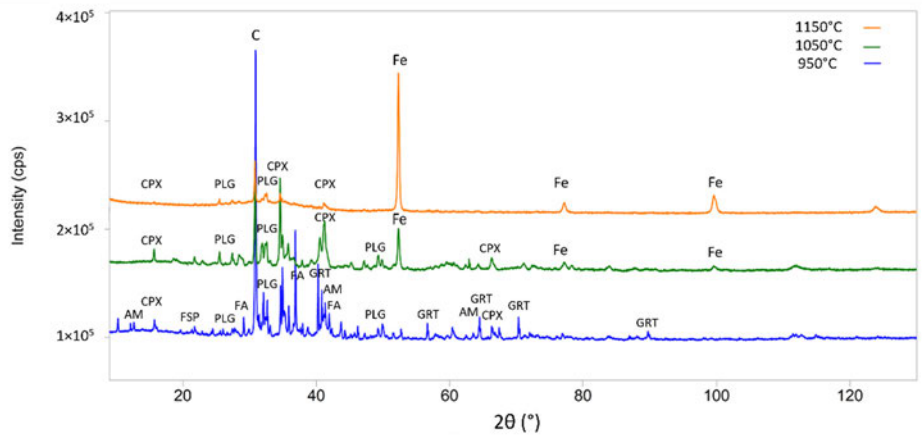


**Fig. 19. XRD patterns of concentrate R3 reduced at temperatures of 950°C, 1050°C, and 1150°C. Mineral abbreviations: AM = amphibole, CPX = clinopyroxene, FA = fayalite, GRT = garnet, PL = plagioclase, FSP = potassium feldspar, C = graphite, Fe = metallic iron (reprinted under CC BY 4.0 license from Paper III © 2022 Authors).**

Binary plots of the main components and $Sc_2O_3$ vs. $SiO_2$ in Figure 20 display the evolution of the chemical composition of the slag phase. As the mineral reactions proceed with increasing temperature, leading eventually to the decomposition and melting of all clinopyroxene, potassic feldspar and plagioclase into the slag by 1250°C, the composition of the slag becomes homogenized with respect to the main components, with a steady decrease in FeO.

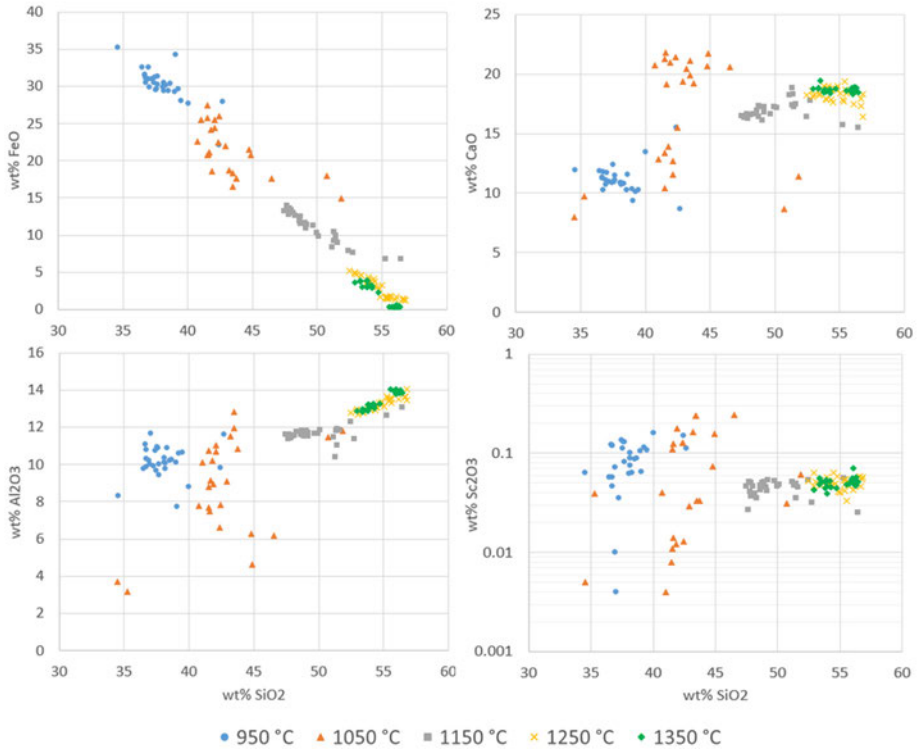


**Fig. 20. Binary plots of FeO, CaO, $Al_2O_3$, and $Sc_2O_3$ (wt%) vs. $SiO_2$ for amphibole relicts (blue) at 950°C and slag at higher temperatures (reprinted under CC BY 4.0 license from Paper III © 2022 Authors).**

With respect to the commonly expressed empirical slag basicity based on $CaO/SiO_2$ (Verein Deustcher Eisenhüttenleute, 1981; Mills et al., 2013), the basicity varied without doping between 0.20 and 0.24, whereas in the doped experiments, it fell in the range of 0.32–0.54. Although still at high acidity and therefore high viscosity, the applied relatively moderate additions of $CaF_2$ and CaO did improve properties via enhanced metal segregation from the slag.

## 6.4 Hydrometallurgical extraction (Paper IV)

Paper IV focuses on hydrometallurgical experiments with respect to the third and final stage of the suggested processing scheme (Figures 1 and 11). Synthetic slag in addition to Kiviniemi R1 and R3 slags were produced for these experiments (details in Paper IV). Figure 21 presents a set of images from slag R1 before final grinding; the remaining small metal in the slag was separated with a hand magnet prior to leaching experiments. The target of grinding was at $D_{90}$ ~30 µm, which was accomplished for the synthetic and R3 slags with 26 and 30 µm, respectively, whereas slag R1 remained slightly coarser with a $D_{90}$ value of 34 µm. Based on slag diffractograms after magnetic separation of the ground slag, the non-magnetic fractions submitted to hydrometallurgical experiments can be considered completely amorphous (details in Paper IV).

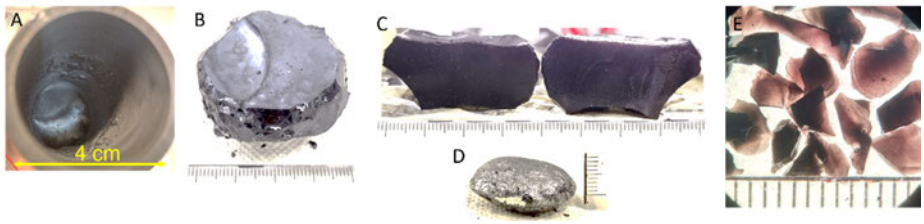


**Fig. 21. Set of images from R1 slag prior to final grinding; (A) slag in the graphite crucible after the reduction; (B) slag cut from the crucible; (C) cross-section of the slag; (D) large metal accumulation; and (E) stereomicroscope image of crushed slag particles (reprinted under CC BY 4.0 license from Paper IV © 2022 Authors).**

Experiments were commenced with dry digestion procedures, but due to the low Sc extraction (≤22 mg $L^{-1}$ after 90 min leaching), focus was soon shifted to $H_2O_2$-assisted $H_2SO_4$ leaching. The factorial design of the experiments is presented in Paper IV. First, the effect of $H_2O_2$ molarity at various levels of $H_2SO_4$ molarity was investigated at 100 °C with S/L of 1:10 on synthetic slag; the highest efficiency of leaching was achieved with the highest molarities of 3.5 M $H_2SO_4$ and 3.5 M $H_2O_2$. Furthermore, the effects of temperature on the leaching efficiency were investigated with an S/L ratio of 1:10 and the effects of varying S/L at 100 °C. The improvement of increasing leaching efficiency with increasing temperature and increasing S/L at 100°C are presented in Figures 22A and 22B, respectively.

Based on the results obtained from the synthetic slag, two levels of acid molarities, 2.5 M $H_2SO_4$ + 2.5 M $H_2O_2$ and 3.5 M $H_2SO_4$ + 3.5 M $H_2O_2$, were selected and used at 100 °C with two ratios of S/L (1:10 and 1:20) for the Kiviniemi

R1 and R3 slags. Figure 23 reveals that there is a significant difference between the leaching characteristics of these two slags, which is considered a consequence of the slightly coarser particle size of R1 slag.

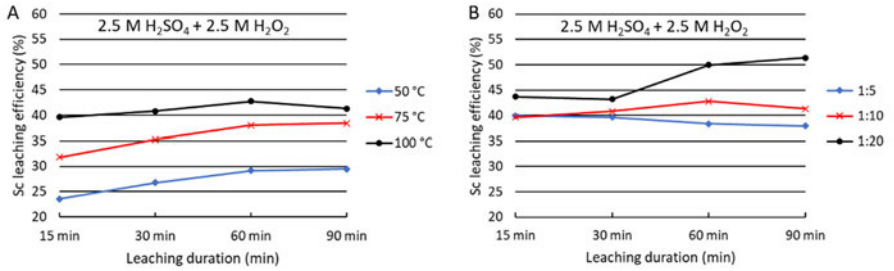


**Fig. 22. Effect of (A) temperature and (B) S/L on Sc leaching efficiency for synthetic slag with 2.5 M $H_2SO_4$ and 2.5 M $H_2O_2$ (reprinted under CC BY 4.0 license from Paper IV © 2022 Authors).**

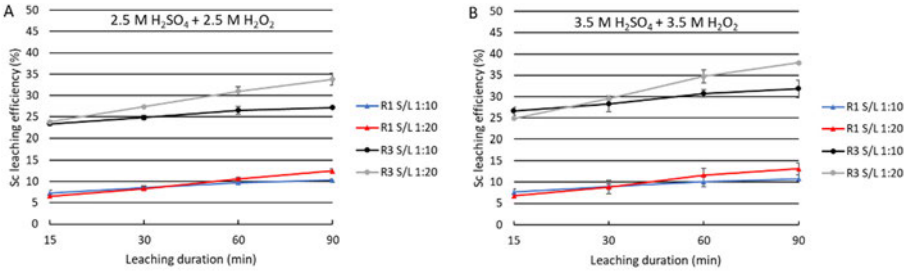


**Fig. 23. Effect of $H_2O_2$ and $H_2SO_4$ molarity and S/L both 1:10 and 1:20 on the leaching efficiency of R1 and R3 slags. (A) 2.5 M $H_2SO_4$ + 2.5 M $H_2O_2$ (B) 3.5 M $H_2SO_4$ + 3.5 M $H_2O_2$. Temperature 100°C. Error bars 2σ (reprinted under CC BY 4.0 license from Paper IV © 2022 Authors).**

Formation of an orange complex was observed as soon as $H_2O_2$ was added into the reactor in all leaching experiments. This is caused by the combined effect of $H_2SO_4$ and $H_2O_2$ contributing to soluble titanium peroxosulfate formation. The formation of soluble titanium peroxosulfate and the mechanism of dissolution in pregnant leach solution (PLS) can be exemplified via the following chemical reactions, in which, at the first-stage, titanium oxide reacts with sulfuric acid to produce oxotitanium sulfate and water (Alkan et al., 2018)

$$TiO_2 + H_2SO_4 \rightarrow [TiO]SO_4 + H_2O \quad (7)$$

$$[TiO]SO_4 + H_2O_2 \rightarrow [TiO\text{-}O]SO_4 + H_2O \quad (8)$$

The secondary electron image of the slag R3 leach residue with corresponding X-ray elemental maps for Si and Ca are shown in Figure 24. Further details on both the EPMA and FESEM-EDS analysis results are provided in Paper IV. Small silica-enriched particles occurring as agglomerates or on the surfaces of larger particles are interpreted to represent essentially a siliceous residue from which other elements have been extracted. Furthermore, silica precipitation under very acidic conditions has been described to proceed via fast polymerization of monomeric silica from solution followed by flocculation (Gorrepati et al., 2010; Voßenkaul et al., 2017); this possibly contributes to the presence of observed $SiO_2$-enriched particles. Although silica precipitation with a crystalline structure has also been suggested as a mechanism for avoiding silica gel formation (Alkan et al., 2018), according to XRD investigations, crystalline silica was not detected.

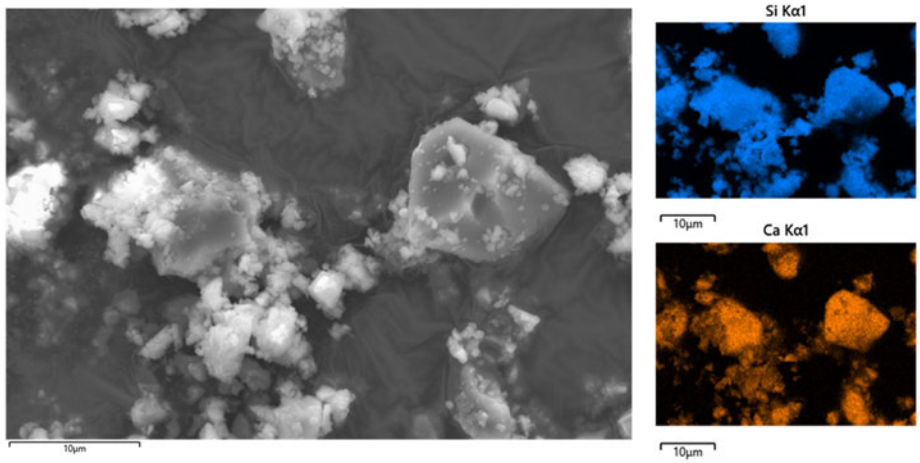


**Fig. 24. Secondary electron image of slag R3 leach residue (2.5 M $H_2O_2$ + 2.5 M $H_2SO_4$ with S/L 1:20 at 100°C) with corresponding X-ray elemental maps for Si and Ca (adapted under CC BY 4.0 license from Paper IV © 2022 Authors).**

Extremely high silica content of the Kiviniemi slags poses challenges compared to hydrometallurgical processing of various slags as based on literature (Alkan et al., 2019; Kim and Azimi, 2020; Perederiy, 2011; Rivera et al., 2019; Yagmurlu et al., 2019). Therefore, focus was given to the suppression of silica gel formation. Even with higher acidity of the Kiviniemi slags (53–56 wt% $SiO_2$ vs. 38; Yagmurlu et al., 2019), smaller particle size distribution of the synthetic reference and R3 slag samples utilized in our experiments allowed reaching 40–50% efficiency of Sc extraction. Despite avoiding silica gel formation under the applied oxidative

leaching conditions, it is obvious that the amorphous structure does not provide the possibility for selective leaching (Figure 25) with respect to other components.

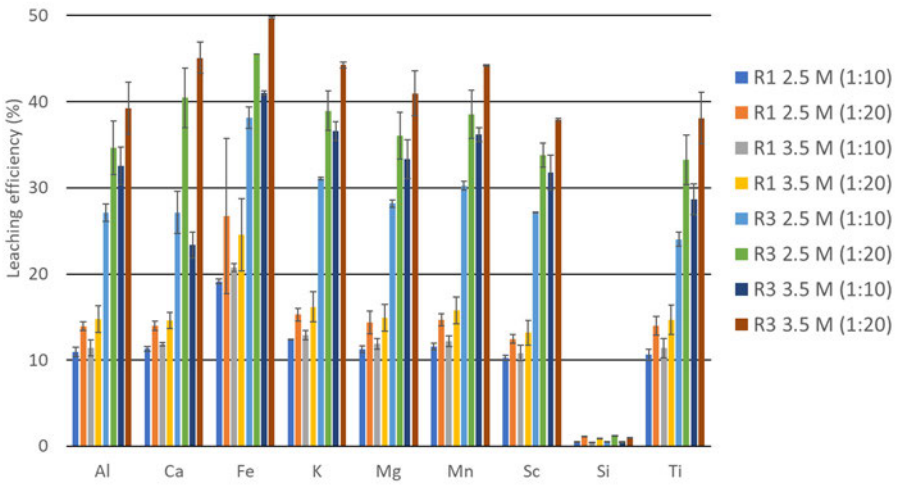


**Fig. 25. Summary of average leaching efficiencies for slags R1 and R3 with both tested molarities and S/L ratios (indicated in brackets) after 90 min of leaching. Based on the compositions of liquids determined by ICP-OES. Error bars 2σ (reprinted under CC BY 4.0 license from Paper IV © 2022 Authors).**

As stated by Terry (1983), in the case of crystalline structures, silica must be present in the leaching material either as units of a small molecular weight to be present to any degree in the solution, or it must be broken into such units by the action of acid. Infinite silicate chains are not easily broken down into smaller silicate units due to the strength of the Si–O bonds, which results as siliceous residue. However, for example $Al_2O_3$ may weaken the silicate network against acid attack. Furthermore, the metal cation–oxygen bond in any silicate material is weaker and more susceptible to acid attack than the silicon–oxygen bond (Terry, 1983). The formation of a passive silica-enriched protective surface layer due to the preferential removal of metal ions (Fe, Mg, Al, Ca, K, Na) by acid has been described in amorphous slag dissolution (Perederiy & Papangelakis, 2017). This is in line with the percolation model of glass dissolution (Cailletau et al., 2008), which results in a siliceous layer due to leaching of alkali and earth alkali cations. Furthermore, according to Perederiy and Papangelakis (2017), hydrolysis of the

Si—O bonds leading to silica dissolution competes with re-polymerization of silica and precipitation of dissolved silicic acid along the path of the acid attack, thus precluding the complete dissolution. This is also interpreted to occur in the Kiviniemi slags; the silica-enriched particles are indications of preferential metal cation dissolution from an amorphous slag. Smaller slag particles respond easily to the acid, whereas larger particles exhibit intact interiors with silica-enriched outer layers as described in more detail in Paper IV.

HPAL leaching of slags after of bauxite residue smelting was studied by Rivera et al. (2019); they reported up to 85 wt% of Sc extraction from amorphous slags using $H_2SO_4$ at 150 °C. Therefore, as the final aspect of hydrometallurgical study, a few HPAL experiments were conducted on synthetic and Kiviniemi R3 slag. However, leaching efficiencies in conditions used in our study remained at lower level (30-45%) than those with atmospheric $H_2O_2$-assisted $H_2SO_4$ leaching. The pressure range (10 and 60 bar) studied in these preliminary experiments appear to have negligible effect to the leaching efficiency for the synthetic reference slag (details in Paper IV).

# 7 Concluding remarks and recommendations for future research

This dissertation consists of four peer-reviewed papers. The first paper focuses on a conventional beneficiation method with mineralogical characterization of Kiviniemi garnet-bearing fayalite ferrodiorite samples included in this study; the next two deal with phenomena related to high-temperature characteristics of the produced concentrates, and the fourth focuses on leaching characteristics of the produced Sc-enriched, Fe-depleted slag. Thus, the samples from Kiviniemi are carried through each suggested processing stage according to the plan introduced in the beginning of this study (Figures 1 and 11), the results combining into a summary on Kiviniemi material properties.

Such a challenging, dispersed element in nature, such as scandium, certainly provides a wide field for experimental research with respect to beneficiation and extraction methods. The characteristics of this element inevitably reflect into the complexity of beneficiation scenarios with no easy solutions in the near future. However, the promising outlook for Sc in high-technology applications, combined with the criticality of the supply, has initiated much research that focuses on its extraction from both primary and secondary sources. This study offers insights into the characteristics of Kiviniemi-type feed material for further evaluation of various processing options. Although this study was conducted along the suggested steps progressing from one to the other, future research can benefit from the results obtained at each step and may include a variety of processing options, also deviating from energy-intensive smelting reduction. It appears obvious that the preconcentration of ferrous scandium carriers with magnetic methods can be considered a sound, feasible, and relatively easy technology, which is easy to implement to a bigger scale. However, the occurrence of Sc as a trace element in clinopyroxene, amphibole, fayalite, and garnet—in other words, in chemically resistant silicate structures—introduces challenges in terms of metal extraction. Furthermore, as observed in this study, overcoming challenges at one stage may give rise to some new ones for the next stages.

If pyrometallurgical treatment is to be considered for Kiviniemi-type ferrous scandium concentrates, one of the difficulties is to optimize and modify the composition of highly viscous slag to promote the reduction of FeO and segregation of metal without excessively diluting the slag $Sc_2O_3$ content. According to the results of this study, the reduction of the ferrous oxide component of the slag and the segregation of metallic iron was improved with moderate additions of $CaF_2$ and

CaO, which lowered the liquidus temperature and viscosity of the slag. Despite the variations in the modal mineralogy of the concentrates used in this study, the high-temperature behavior essentially remained similar, although the main reduction stage is initiated at a slightly higher temperature (~1000–1030°C) for the concentrates with less amphibole and a higher amount of nonferrous minerals. The beginning of the main reduction stage, with the formation of initial slag, is dominated by the decomposition and reduction of amphibole and garnet. The final decomposition of clinopyroxene occurs at a significantly higher temperature than that of amphibole, with structures persisting until 1150°C. Only after the complete melting of silicates and dissolution of unreduced FeO into the slag can the final FeO reduction from the slag be achieved by carbon, accompanied by segregation and accumulation of metallic iron.

Although pyrometallurgy does offer the potential to eliminate what could be stated as the "Fe problem" for the hydrometallurgical extraction and separation stages, the benefits of pyrometallurgical processing against the drawbacks of high energy consumption would have to be carefully evaluated. If pyrometallurgy continues to be included as an option for the Kiviniemi-type feed material, the effects of hydrogen on reduction should be investigated. Unfortunately, this was not possible in this study, whereas recently upgraded research infrastructure at the Process Metallurgy Research unit would allow these types of studies to be conducted in the future. Furthermore, other options might be provided by milder, high-temperature manipulation of the concentrate crystalline structures without smelting reduction. A somewhat similar analog, which has been used in industrial production, is roasting of ilmenomagnetite with sodium carbonate to recover vanadium via the formation of soluble sodiumvanadate—then again, extracting elements from oxide lattices is a simpler task than extracting trace elements from silicate lattices, and particularly for an element with an ability to change oxidation state, unlike scandium. Moreover, $Ca(OH)_2$-coal roasting procedures to recover iron, niobium, and scandium from the Bayan Obo tailings, followed by sulfuric acid leaching process, have been reported (Zhang et al., 2019). Although Sc occurs mainly in pyroxene and possibly amphibole in the Bayan Obo tailings, the differences in feed mineralogy might hinder the possibilities offered by roasting in the case of Kiviniemi. Among the pyrometallurgical options, controlled cooling procedures with or without further slag modification might provide crystalline material for the hydrometallurgical stage. The phenomena related to the leaching characteristics of feed material are strongly influenced by the type of crystalline structures involved. Therefore, crystalline structures may provide the benefit of

selective or enhanced leaching; however, excessive dilution of the slag $Sc_2O_3$ content in the case of further compositional modification should be avoided.

Although slag systems have been reported to have high Sc leaching efficiencies with mineral acids, it appears obvious that the Kiviniemi slag system as such does not offer any easy solutions for sufficiently high extraction efficiencies, which remained in the range of 40–50%. Nevertheless, hydrometallurgical processing options provide a huge field for investigation, and most likely there are several options for both concentrate and pyrometallurgically treated materials with which studies can be continued. The process of direct hydrometallurgical extraction from magnetic concentrates is currently under development with a similar type of primary Sc resource, Crater Lake in Canada, focusing on a two-stage extraction method with a high-pressure caustic leach (HPC), followed by hydrochloric acid leach of the HPC residue. The separation of Sc products after this type of extraction is not yet published; however, it should consider having a control over soluble Fe, which is known to deteriorate the Sc separation.

Understanding and characterizing the behavior of material, as dictated by mineralogy, is the basis for any developmental work aiming toward beneficiation. The results of this study provide information for further studies of the beneficiation potential of Kiviniemi-type deposits, where Sc is incorporated in ferrous silicate minerals. Whether technological pull will be sufficient to allow more studies on the development of beneficiation of the Kiviniemi deposit, remains to be seen.

# References


Ahmad, Z. (2003). The properties and application of scandium-reinforced aluminum. *The Journal of The Minerals, Metals & Materials Society (TMS)*, *55*, 35–39.

Akcil, A., Akhmadiyeva, N., Abdulvaliyev, R., Abhilash, & Meshram, P. (2018). Overview on extraction and separation of rare earth elements from red mud: Focus on scandium. *Mineral Processing and Extractive Metallurgy Review*, *39*(3), 145–151. https://doi.org/10.1080/08827508.2017.1288116

Alkan, G., Schier, C., Gronen, L., Stopic, S., & Friedrich, B. (2017). A mineralogical assessment on residues after acidic leaching of bauxite residue (Red mud) for titanium recovery. *Metals*, *7*(11). https://doi.org/10.3390/met7110458

Alkan, G., Yagmurlu, B., Cakmakoglu, S., Hertel, T., Kaya, Ş., Gronen, L., Stopic, S., & Friedrich, B. (2018). Novel approach for enhanced scandium and titanium leaching efficiency from bauxite residue with suppressed silica gel formation. *Scientific Reports*, *8*(1), 1–12. https://doi.org/10.1038/s41598-018-24077-9

Alkan, G., Yagmurlu, B., Gronen, L., Dittrich, C., Ma, Y., Stopic, S., & Friedrich, B. (2019). Selective silica gel free scandium extraction from iron-depleted red mud slags by dry digestion. *Hydrometallurgy*, *185*(March), 266–272. https://doi.org/10.1016/j.hydromet.2019.03.008

Anawati, J., & Azimi, G. (2022). Integrated carbothermic smelting – acid baking – water leaching process for extraction of scandium, aluminum, and iron from bauxite residue. *Journal of Cleaner Production*, *330*(November 2021), 129905. https://doi.org/10.1016/j.jclepro.2021.129905

Aparicio, C., Filip, J., & Mashlan, M. (2010). High temperature decomposition of almandine and pyrope in reducing atmosphere. *AIP Conference Proceedings*, *1258*(May 2014), 47–54. https://doi.org/10.1063/1.3473898

Baghalha, M., Papangelakis, V. G., & Curlook, W. (2007). Factors affecting the leachability of Ni/Co/Cu slags at high temperature. *Hydrometallurgy*, *85*(1), 42–52. https://doi.org/10.1016/j.hydromet.2006.07.007

Bédard, J. H. (2014). Parameterizations of calcic clinopyroxene - Melt trace element partition coefficients. *Geochemistry, Geophysics, Geosystems*, *15*(2), 303–336. https://doi.org/10.1002/2013GC005112

Begoc, S., Montredon, F., Pommatau, G., Leger, G., Gas, M., & Eyrignoux, S. (2019). Additive manufacturing of Scalmalloy® satellite parts. *Proceedings of the 8th European Conference for Aeronautics and Space Sciences (EUCASS)*, 1–15. https://doi.org/10.13009/EUCASS2019-677

Beland, C. M. J. (2021). *The contrasting geochemical behaviour of Sc and the other REE as exemplified by the Crater Lake and Ashram deposits, Québec, Canada* (Issue April). McGill Univeristy, Montreal.

Binnemans, K., Jones, P. T., Blanpain, B., Van Gerven, T., & Pontikes, Y. (2015). Towards zero-waste valorisation of rare-earth-containing industrial process residues: A critical review. *Journal of Cleaner Production*, *99*, 17–38. https://doi.org/10.1016/j.jclepro.2015.02.089

Bisaka, K., Thobadi, I. C., & Pawlik, C. (2017). Extraction of rare earths from iron-rich rare earth deposits. *Journal of the Southern African Institute of Mining and Metallurgy*, *117*(8), 731–739. https://doi.org/10.17159/2411-9717/2017/v117n8a2

Blengini, G. A., El Latunussa, C., & Eynard, U. (2020). Study on the EU's list of critical raw materials (2020) - critical raw materials factsheets. In *Critical Raw Materials Factsheets*. https://doi.org/10.2873/92480

Bobba, S., Carrara, S., Huisman, J., Mathieux, F., & Pavel, C. (2020). Critical raw materials for strategic technologies and sectors in the EU - a foresight study. In *European Commission*. https://doi.org/10.2873/58081

Borra, C. R., Pontikes, Y., Binnemans, K., & Van Gerven, T. (2015). Leaching of rare earths from bauxite residue (red mud). *Minerals Engineering*, *76*, 20–27. https://doi.org/10.1016/j.mineng.2015.01.005

Botelho Junior, A. B., Espinosa, D. C. R., Vaughan, J., & Tenório, J. A. S. (2021). Recovery of scandium from various sources: A critical review of the state of the art and future prospects. *Minerals Engineering*, *172*(May), 1–20. https://doi.org/10.1016/j.mineng.2021.107148

Brett, B. N. H., Mackenzie, K. J. D., & Sharp, J. H. (1970). The thermal decomposition of hydrous layer silicates and their related hydroxides. *Quarterly Review of the Chemical Society*, *2*, 185–207.

Brown, M. E. (2004). *Introduction to thermal analysis*. Kluwer Academic Publishers.

Bueno, M., Torvela, J., Chandramohan, R., Chavez Matus, T., Liedes, T., & Powell, M. (2021). The double wheel breakage test. *Minerals Engineering*, *168*(June 2020), 106905. https://doi.org/10.1016/j.mineng.2021.106905

Cai, J., Xu, D., Dong, Z., Yu, X., Yang, Y., Banks, S. W., & Bridgwater, A. V. (2018). Processing thermogravimetric analysis data for isoconversional kinetic analysis of lignocellulosic biomass pyrolysis: Case study of corn stalk. *Renewable and Sustainable Energy Reviews*, *82*(October 2017), 2705–2715. https://doi.org/10.1016/j.rser.2017.09.113

Cailletau, C., Weigel, C., Ledieu, A., Barboux, P., & Devreus, F. (2008). On the effect of glass composition in the dissolution of glasses by water. *Journal of Non-Crystalline Sollids*, *354*, 117–123. https://doi.org/10.1016/j.jnoncrysol.2007.07.063

Chassé, M., Griffin, W. L., Alard, O., O'Reilly, S. Y., & Calas, G. (2018). Insights into the mantle geochemistry of scandium from a meta-analysis of garnet data. *Lithos*, *310–311*, 409–421. https://doi.org/10.1016/j.lithos.2018.03.026

Chassé, M., Griffin, W. L., O'Reilly, S. Y., & Calas, G. (2017). Scandium speciation in a world-class lateritic deposit. *Geochemical Perspectives Letters*, *3*(2), 105–114. https://doi.org/10.7185/geochemlet.1711

Chassé, M., Griffin, W. L., O'Reilly, S. Y., & Calas, G. (2019). Australian laterites reveal mechanisms governing scandium dynamics in the critical zone. *Geochimica et Cosmochimica Acta*, *260*, 292–310. https://doi.org/10.1016/j.gca.2019.06.036

Chen, L., & Xiong, D. (2015). Magnetic techniques for mineral processing. In *Progress in Filtration and Separation*. Elsevier Ltd. https://doi.org/10.1016/B978-0-12-384746-1.00007-0

Connelly, N. G., Hartshorn, R. M., Damhus, T., & Hutton, A. T. (2005). Nomenclature of inorganic chemistry IUPAC recommendations 2005. In *Royal Society of Chemistry* (Vol. 128, Issue 21). RSC Publishing.

Dobbins, M., Dunn, P., & Sherrell, I. (2009). Recent advances in magnetic separator designs and applications. *The 7th International Heavy Minerals Conference*, 63–70.

Dorin, T., Ramajayam, M., Vahid, A., & Langan, T. (2018). Aluminium scandium alloys. In *Fundamentals of Aluminium Metallurgy*. Elsevier Ltd. https://doi.org/10.1016/b978-0-08-102063-0.00012-6

Dunne, R.C., Honaker, R.Q., Giblett, A. (2019). Gravity concentration. In S. K. Kawatra, C., Young (Ed.), *SME mineral processing and extractive metallurgy handbook* (pp. 787–814). Society for Mining, Metallurgy and Exploration.

Duyvesteyn, W., & Putnam, G. (2014). *Scandium, a review of the element, its characteristics, and current and emerging commercial applications [White paper]*.

Eilu, P. (2017). Critical raw materials factsheets. *European Commision*, *June*, 515. https://doi.org/10.2873/398823

EIT Raw Materials. (2022). *ScaVanger: Sustainable supply of Nb, Sc and V from liquid waste from TiO2 plants*. https://eitrawmaterials.eu/project/scavanger/

Fan, H. R., Yang, K. F., Hu, F. F., Liu, S., & Wang, K. Y. (2016). The giant Bayan Obo REE-Nb-Fe deposit, China: Controversy and ore genesis. *Geoscience Frontiers*, *7*(3), 335–344. https://doi.org/10.1016/j.gsf.2015.11.005

Faris, N., Ram, R., Tardio, J., Bhargava, S., McMaster, S., & Pownceby, M. I. (2017). Application of ferrous pyrometallurgy to the beneficiation of rare earth bearing iron ores – A review. *Minerals Engineering*, *110*(February), 20–30. https://doi.org/10.1016/j.mineng.2017.04.005

Foldvari, M. (2011). Handbook of thermo-gravimetric system of minerals and its use in geological practice. In *Occasional papers of the geological institute of Hungary* (Vol. 213). Geological Institute of Hungary.

Gion, A. M., Piccoli, P. M., Fei, Y., Candela, P. A., & Ash, R. D. (2021). Experimental constraints on the formation of pegmatite-forming melts by anatexis of amphibolite: A case study from Evje-Iveland, Norway. *Lithos*, *398–399*(July), 106342. https://doi.org/10.1016/j.lithos.2021.106342

Goode, J. R. (2019). Rare earth elements. In *SME mineral processing and extractive metallurgy handbook* (pp. 2049–2075). Society for Mining, Metallurgy and Exploration.

Gorrepati, E. A., Wongthahan, P., Raha, S., & Fogler, H. S. (2010). Silica precipitation in acidic solutions: mechanism, pH effect, and salt effect. *Langmuir*, *26*(14), 10467–10474. https://doi.org/10.1021/la904685x

Gramaccioli, C. M., Diella, V., & Demartin, F. (2000). The formation of scandium minerals as an example of the role of complexes in the geochemistry of rare earths and HFS elements. *European Journal of Mineralogy*, *12*(4), 795–808. https://doi.org/10.1127/ejm/12/4/0795

Grapes, R. (2006). Pyrometamorphism. In *Pyrometamorphism* (Second edi). Springer. https://doi.org/10.1007-978-3-642-15588-8

Gupta, G. K., & Krishnamurthy, N. (2005). Extractive metallurgy of rare earths. In *Extractive metallurgy of rare earths* (Vol. 37, Issue 1). CRC Press. https://doi.org/10.1179/imr.1992.37.1.197

Halkoaho, T., Ahven, M., Rämö, O. T., Hokka, J., & Huhma, H. (2020). Petrography, geochemistry and geochronoloy of the Sc-enriched Kiviniemi ferrodiorite intrusion, eastern Finland. *Mineralium Deposita*, 1–20. https://doi.org/https://doi.org/10.1007/s00126-020-00952-2

Haque, N., Hughes, A., Lim, S., & Vernon, C. (2014). Rare earth elements: Overview of mining, mineralogy, uses, sustainability and environmental impact. *Resources*, *3*(4), 614–635. https://doi.org/10.3390/resources3040614

Henderson, P. (1984). General geochemical properties and abundances of the rare earth elements. In *Rare Earth Element Geochemistry* (pp. 1–32). Elsevier. https://doi.org/10.1016/b978-0-444-42148-7.50006-x

Hill, E., Blundy, J. D., & Wood, B. J. (2011). Clinopyroxene-melt trace element partitioning and the development of a predictive model for HFSE and Sc. *Contributions to Mineralogy and Petrology*, *161*(3), 423–438. https://doi.org/10.1007/s00410-010-0540-0

Hodgson, A. A., Freeman, A. G., & Taylor, H. F. W. (1965). The thermal decomposition of amosite. *Mineralogical Magazine and Journal of the Mineralogical Society*, *35*(271), 445–463. https://doi.org/10.1180/minmag.1965.035.271.01

Hokka, J., & Halkoaho, T. (2016). *3D modelling and mineral resource estimation of the Kiviniemi Scandium deposit, Eastern Finland* (Issue January). https://doi.org/10.13140/RG.2.2.25709.18400

Horovitz, C. T., Gschneidner, Jr, K. A., Melson, G. A., Youngblood, D. H., S. H. H. (1975). *Scandium: its occurrence, chemistry, physics, metallurgy, biology and technology*. Academic Press Inc. (London) Ltd.

Hunt, C. P., Moskowitz, B. M., & Banerjee, S. K. (1995). Magnetic properties of rocks and minerals. In T. J. Ahrens (Ed.), *Rock Physics and Phase Relations A Handbook of Physical Constants* (AGU Refere, pp. 189–204). American Geophysical Union. https://doi.org/10.1016/B978-0-444-53802-4.00048-8

Imperial Mining Group Ltd. (2022). *Crater Lake*. https://imperialmgp.com/projects/crater-lake/

Ishiwatari, A., & Ichiyama, Y. (2004). Alaskan-type plutons and ultramafic lavas in Far East Russia, Northeast China, and Japan. *International Geology Review*, *46*(4), 316–331. https://doi.org/10.2747/0020-6814.46.4.316

Jaireth, S., Hoatson, D. M., & Miezitis, Y. (2014). Geological setting and resources of the major rare-earth-element deposits in Australia. *Ore Geology Reviews*, *62*, 72–128. https://doi.org/10.1016/j.oregeorev.2014.02.008

Jordens, A., Cheng, Y. P., & Waters, K. E. (2013). A review of the beneficiation of rare earth element bearing minerals. *Minerals Engineering*, *41*, 97–114. https://doi.org/10.1016/j.mineng.2012.10.017

Jung, I. H., & Van Ende, M. A. (2020). Computational thermodynamic calculations: FactSage from CALPHAD Thermodynamic Database to virtual process simulation. *Metallurgical and Materials Transactions B: Process Metallurgy and Materials Processing Science*, *51*(5), 1851–1874. https://doi.org/10.1007/s11663-020-01908-7

Kaia, T., Gross, K., & Veiderma, M. (2012). *A review on the thermal stability of calcium apatites*. *110*(November), 647–659. https://doi.org/10.1007/s10973-011-1877-y

Kalashnikov, A. O., Yakovenchuk, V. N., Pakhomovsky, Y. A., Bazai, A. V., Sokharev, V. A., Konopleva, N. G., Mikhailova, J. A., Goryainov, P. M., & Ivanyuk, G. Y. (2016). Scandium of the Kovdor baddeleyite-apatite-magnetite deposit (Murmansk Region, Russia): Mineralogy, spatial distribution, and potential resource. *Ore Geology Reviews*, *72*(P1), 532–537. https://doi.org/10.1016/j.oregeorev.2015.08.017

Kato, M., & Minowa, S. (1969). Viscosity measurements of molten slag. *Transactions ISIJ*, *9*(Part 1), 31–38.

Kekkonen, M., Oghbasilasie, H., & Louhenkilpi, S. (2012). *Viscosity models for molten slags*.

Kennedy, M. W., Sun, T., Yurramendi, L., Arnout, S., Aune, R. E., & Tranell, G. (2017). Pyrometallurgical treatment of apatite concentrate with the objective of rare earth element recovery: Part II. *Journal of Sustainable Metallurgy*, *3*(4), 846–857. https://doi.org/10.1007/s40831-017-0148-y

Khanna, R., Konyukhov, Y., Zinoveev, D., Jayasankar, K., Burmistrov, I., Kravchenko, M., & Mukherjee, P. S. (2022). Red mud as a secondary resource of low-grade iron: A global perspective. *Sustainability (Switzerland)*, *14*(3). https://doi.org/10.3390/su14031258

Kim, J., & Azimi, G. (2020). Recovery of scandium and neodymium from blast furnace slag using acid baking-water leaching. *RSC Advances*, *10*(53), 31936–31946. https://doi.org/10.1039/d0ra05797e

Kondratiev, A., Jak, E., & Hayes, P. C. (2002). Predicting slag viscosities in metallurgical systems. *Jom*, *54*(11), 41–45. https://doi.org/10.1007/BF02709749

Korhonen, T., Neitola, R., Mörsky, P., & Laukkanen, J. (2011). *Alustavia skandiumin rikastustutkimuksia Rautalammin Kiviniemen näytteellä*. https://tupa.gtk.fi/raportti/arkisto/mt_2010_56.pdf

Kracek, F. C. (1963). Contributions to geochemistry: melting and transformation temperatures of mineral and allied substances. *Geological Survey Bulletin 1144-D*, 88.

Krause, J., Brügmann, G. E., & Pushkarev, E. V. (2007). Accessory and rock forming minerals monitoring the evolution of zoned mafic-ultramafic complexes in the Central Ural Mountains. *Lithos*, *95*(1–2), 19–42. https://doi.org/10.1016/j.lithos.2006.07.018

Lapin, A. V., Tolstov, A. V., & Kulikova, I. M. (2016). Distribution of REE, Y, Sc, and Th in the unique complex rare-metal ores of the Tomtor deposit. *Geochemistry International*, *54*(12), 1061–1078. https://doi.org/10.1134/S0016702916120065

Lathabai, S., & Lloyd, P. G. (2002). The effect of scandium on the microstructure, mechanical properties and weldability of a cast Al-Mg alloy. *Acta Materialia*, *50*(17), 4275–4292. https://doi.org/10.1016/S1359-6454(02)00259-8

Lee, Y. E., & Kolbeinsen, L. (2021). Behavior of slag in ferromanganese and silicomanganese smelting process. *Metallurgical and Materials Transactions B: Process Metallurgy and Materials Processing Science*, *52*(5), 3142–3150. https://doi.org/10.1007/s11663-021-02242-2

Leißner, T., Bachmann, K., Gutzmer, J., & Peuker, U. A. (2016). MLA-based partition curves for magnetic separation. *Minerals Engineering*, *94*, 94–103. https://doi.org/10.1016/j.mineng.2016.05.015

Li, G., Liu, M., Rao, M., Jiang, T., Zhuang, J., & Zhang, Y. (2014). Stepwise extraction of valuable components from red mud based on reductive roasting with sodium salts. *Journal of Hazardous Materials*, *280*, 774–780. https://doi.org/10.1016/j.jhazmat.2014.09.005

Li, G., Ye, Q., Deng, B., Luo, J., Rao, M., Peng, Z., & Jiang, T. (2018). Extraction of scandium from scandium-rich material derived from bauxite ore residues. *Hydrometallurgy*, *176*(December 2017), 62–68. https://doi.org/10.1016/j.hydromet.2018.01.007

Li, Y. (2018). Temperature and pressure effects on the partitioning of v and Sc between clinopyroxene and silicate melt: Implications for mantle oxygen fugacity. *American Mineralogist*, *103*(5), 819–823. https://doi.org/10.2138/am-2018-6464

Li, Y., Papangelakis, V. G., & Perederiy, I. (2009). High pressure oxidative acid leaching of nickel smelter slag: Characterization of feed and residue. *Hydrometallurgy*, *97*(3–4), 185–193. https://doi.org/10.1016/j.hydromet.2009.03.007

Liu, Z., & Li, H. (2015). Metallurgical process for valuable elements recovery from red mud - A review. *Hydrometallurgy*, *155*, 29–43. https://doi.org/10.1016/j.hydromet.2015.03.018

Mallmann, G., & O'Neill, H. S. C. (2009). The crystal/melt partitioning of V during mantle melting as a function of oxygen fugacity compared with some other elements (Al, P, Ca, Sc, Ti, Cr, Fe, Ga, Y, Zr and Nb). *Journal of Petrology*, *50*(9), 1765–1794. https://doi.org/10.1093/petrology/egp053

Maroufi, S., Ciezki, G., Jahanshahi, S., & Ostrovski, O. (2016). Carbothermal reduction of iron and silicon oxides in ironstone ore. *Transactions of the Institutions of Mining and Metallurgy, Section C: Mineral Processing and Extractive Metallurgy*, *125*(2), 86–94. https://doi.org/10.1080/03719553.2016.1156800

Martin, L. H. J., Schmidt, M. W., Mattsson, H. B., & Guenther, D. (2013). Element partitioning between immiscible carbonatite and silicate melts for dry and H2O-bearing systems at 1-3GPa. *Journal of Petrology*, *54*(11), 2301–2338. https://doi.org/10.1093/petrology/egt048

Massieon, C. C., Cutler, A. H., & Shadmanv, F. (1993). Hydrogen reduction of iron-bearing silicates. *Industrial & Engineering Chemistry Research*, *32*(6), 1239–1244.

Massieon, C., Cutler, A., & Shadman, F. (1992). *Reduction of iron-bearing lunar minerals for the production of oxygen* (Vols. N93-26676).

Metso Outotec. (2022). *SLon® vertically pulsating high- gradient magnetic separator*. https://www.mogroup.com/portfolio/vertically-pulsating-high-gradient-magnetic-separator/

Mills, K. C., Hayashi, M., Wang, L., & Watanabe, T. (2013). The structure and properties of silicate slags. In *Treatise on Process Metallurgy* (Vol. 1). Elsevier Ltd. https://doi.org/10.1016/B978-0-08-096986-2.00008-4

Milman, Y. V. (2006). Scandium effect on increasing mechanical properties of aluminum alloys. *High Temperature Materials and Processes*, *25*(1–2), 1–10. https://doi.org/10.1515/HTMP.2006.25.1-2.1

Minor Metals Trade Association. (2022). *Scandium emerges from the shadows*. https://mmta.co.uk/2022/04/05/scandium-emerges-from-the-shadows/

Moreira, A. Si. B., Silva, C. A., & Silva, I. A. (2018). Replacement of fluorspar in the desulphurization of hot metal. *Metallurgy and Materials*, *71*(2), 261–267.

Nakamoto, M., Tanaka, T., Holappa, L., & Hämäläinen, M. (2007). Surface tension evaluation of molten silicates containing surface-active components (B2O3, CaF2 or Na2O). *ISIJ International*, *47*(2), 211–216. https://doi.org/10.2355/isijinternational.47.211

Nandedkar, R. H., Ulmer, P., & Müntener, O. (2014). Fractional crystallization of primitive, hydrous arc magmas: An experimental study at 0.7 GPa. *Contributions to Mineralogy and Petrology*, *167*(6), 1–27. https://doi.org/10.1007/s00410-014-1015-5

Nordman, T., & Kuusisto, M. (1994). *Application of high intensity magnetic separation for the beneficiation of Finnish metal and industrial mineral ores* (Vuorimiesyhdistys (Ed.); Series A). Vuorimiesyhdistys.

Norman, J. C., & Haskin, L. A. (1968). The geochemistry of Sc: A comparison to the rare earths and Fe. *Geochimica et Cosmochimica Acta*, *32*(1), 93–108. https://doi.org/10.1016/0016-7037(68)90089-6

Park, J. H., Min, D. J., & Song, H. S. (2004). Amphoteric behavior of alumina in viscous flow and structure of CaO-SiO2 (-MgO)-Al2O3 slags. *Metallurgical and Materials Transactions B: Process Metallurgy and Materials Processing Science*, *35*(2), 269–275. https://doi.org/10.1007/s11663-004-0028-2

Pearson, R. G. (1963). Hard and soft acids and bases. *Journal of the American Chemical Society*, *85*(22), 3533–3539.

Penttilä, K. (2014). Modelling of thermophysical properties in EAF-process and steelmaking. In *VTT report* (Issue VTT-R-01304-12).

Perederiy, I. (2011). *Dissolution of valuable metals from nickel smelter slags by means of high pressure oxidative acid leaching*. University of Toronto.

Perederiy, I., & Papangelakis, V. G. (2017). Why amorphous FeO-SiO2 slags do not acid-leach at high temperatures. *Journal of Hazardous Materials*, *321*, 737–744. https://doi.org/10.1016/j.jhazmat.2016.09.055

Perejón, A., Sánchez-Jiménez, P. E., Criado, J. M., & Pérez-Maqueda, L. A. (2011). Kinetic analysis of complex solid-state reactions. A new deconvolution procedure. *Journal of Physical Chemistry B*, *115*(8), 1780–1791. https://doi.org/10.1021/jp110895z

Persson, M., Seetharaman, S., & Seetharaman, S. (2007). Kinetic studies of fluoride evaporation from slags. *ISIJ International*, *47*(12), 1711–1717. https://doi.org/10.2355/isijinternational.47.1711

Petrella, L., Williams-Jones, A. E., Goutier, J., & Walsh, J. (2014). The nature and origin of the rare earth element mineralization in the misery syenitic intrusion, Northern Quebec, Canada. *Economic Geology*, *109*(6), 1643–1666. https://doi.org/10.2113/econgeo.109.6.1643

Pirajno, F., Mao, J., Zhang, Z., Zhang, Z., & Chai, F. (2008). The association of mafic-ultramafic intrusions and A-type magmatism in the Tian Shan and Altay orogens, NW China: Implications for geodynamic evolution and potential for the discovery of new ore deposits. *Journal of Asian Earth Sciences*, *32*(2–4), 165–183. https://doi.org/10.1016/j.jseaes.2007.10.012

Queneau, P. B., & Berthold, C. E. (1986). Silica in hydrometallurgy: An overview. *Canadian Metallurgical Quarterly*, *25*(3), 201–209. https://doi.org/10.1179/000844386795430270

Radzikowska, J. M. (2017). Metallography and microstructures of cast iron[1]. *Cast Iron Science and Technology*, 565–587. https://doi.org/10.31399/asm.hb.v01a.a0006342

Rangott, M., Hutchin, S., Basile, D., Ricketts, N., Duckworth, G., & Rowles, T. D. (2016). Feasibility study-Nyngan Scandium Project. In *Scandium Internaional Mining Corp.*

Ray, N., Nayak, D., Dash, N., & Rath, S. S. (2018). Utilization of low-grade banded hematite jasper ores: Recovery of iron values and production of ferrosilicon. *Clean Technologies and Environmental Policy*, *20*(8), 1761–1771. https://doi.org/10.1007/s10098-018-1566-7

Rio Tinto. (2022). *Rio Tinto becomes the first producer of scandium oxide in North America*. https://www.riotinto.com/news/releases/2022/Rio-Tinto-becomes-the-first-producer-of-scandium-oxide-in-North-America

Riva, S., Yusenko, K. V., Lavery, N. P., Jarvis, D. J., & Brown, S. G. R. (2016). The scandium effect in multicomponent alloys. *International Materials Reviews*, *61*(3), 203–228. https://doi.org/10.1080/09506608.2015.1137692

Rivera, R. M., Ulenaers, B., Ounoughene, G., Binnemans, K., & Van Gerven, T. (2018). Extraction of rare earths from bauxite residue (red mud) by dry digestion followed by water leaching. *Minerals Engineering*, *119*(February), 82–92. https://doi.org/10.1016/j.mineng.2018.01.023

Rivera, R. M., Xakalashe, B., Ounoughene, G., Binnemans, K., Friedrich, B., & Van Gerven, T. (2019). Selective rare earth element extraction using high-pressure acid leaching of slags arising from the smelting of bauxite residue. *Hydrometallurgy*, *184*(December 2018), 162–174. https://doi.org/10.1016/j.hydromet.2019.01.005

Rosenblum, S., & Brownfield, I. (2000). Magnetic susceptibilities of minerals. *Open File Report 99-529*, 1–37. https://doi.org/10.3133/ofr99529

Royset, J. (2007). Scandium in aluminium alloys overview: Physical metallurgy, properties and applications. *Metallurgical Science and Technology*, *25*(2), 11–21.

Saadatkhah, N., Carillo Garcia, A., Ackermann, S., Leclerc, P., Latifi, M., Samih, S., Patience, G. S., & Chaouki, J. (2020). Experimental methods in chemical engineering: Thermogravimetric analysis—TGA. *Canadian Journal of Chemical Engineering*, *98*(1), 34–43. https://doi.org/10.1002/cjce.23673

Safarian, J., Kolbeinsen, L., Tangstad, M., & Tranell, G. (2009). Kinetics and mechanism of the simultaneous carbothermic reduction of FeO and MnO from high-carbon ferromanganese slag. *Metallurgical and Materials Transactions B: Process Metallurgy and Materials Processing Science*, *40*(6), 929–939. https://doi.org/10.1007/s11663-009-9294-3

Sahama, T. G. (1947). *Geokemia*. Otava.

Samson, I., & Chassé, M. (2016). Scandium (Sc). In W. White (Ed.), *Encyclopedia of geochemistry* (Encycloped, Issue January, pp. 1–5). Springer. https://doi.org/10.1007/978-3-319-39193-9_281-1

Sarma, B., Cramb, A. W., & Fruehan, R. J. (1996). Reduction of FeO in smelting slags by solid carbon: Experimental results. *Metallurgical and Materials Transactions B: Process Metallurgy and Materials Processing Science*, *27*(5), 717–730. https://doi.org/10.1007/BF02915600

Schrödle, S., Wachter, W., Buchner, R., & Hefter, G. (2008). Scandium sulfate complexation in aqueous solution by dielectric relaxation spectroscopy. *Inorganic Chemistry*, *47*(19), 8619–8628. https://doi.org/10.1021/ic702396r

Schwab, G. M., & Philinis, J. (1947). Reactions of iron pyrite: Its thermal decomposition, reduction by hydrogen and air oxidation. *Journal of the American Chemical Society*, *69*(11), 2588–2596. https://doi.org/10.1021/ja01203a007

Seetharaman, S. (Ed.). (2005). *Fundamentals of metallurgy*. Woodhead Publishing Limited and CRC Press LCC.

Seetharaman, S., Mukai, K., & Sichen, D. (2005). Viscosities of slags - An overview. *Steel Research International*, *76*(4), 267–278. https://doi.org/10.1002/srin.200506008

Shannon, R. D. (1976). Revised effective ionic radii and systematic studies of interatomic distances in halides and chalcogenides. *Acta Crystallographica Section A*, *32*(5), 751–767. https://doi.org/10.1107/S0567739476001551

Shchekina, T. I., & Gramenitskii, E. N. (2008). Geochemistry of Sc in the magmatic process: Experimental evidence. *Geochemistry International*, *46*(4), 351–366. https://doi.org/10.1134/S0016702908040046

Siddiqi, N., Sahajwalla, V., Ostrovski, O., & Belton, G. R. (1997). Wettability of graphite by CaO-SiO2-Al2O3-FeO-MgO slag. *High Temperature Materials and Processes*, *16*(4), 213–225. https://doi.org/10.1515/HTMP.1997.16.4.213

Stefanescu, D. M., Alonso, G., Larrañaga, P., De la Fuente, E., & Suarez, R. (2018). A comparative study of graphite growth in cast iron and in analogous systems. *International Journal of Metalcasting*, *12*(4), 722–752. https://doi.org/10.1007/s40962-017-0204-1

Svoboda, J. (2004). *Magnetic techniques for the treatment of materials*. Kluwer Academic Publishers.

Tangstad, M. (2013). Ferrosilicon and silicon technology. In *Handbook of Ferroalloys* (12th Ed). Elsevier. https://doi.org/10.1016/B978-0-08-097753-9.00006-X

Taylor, S. . (1964). Abundance of chemical elements in the continental crust : a new table. *Geochimica et Cosmochimica Acta*, *28*, 1273–1285.

Teasdale, S. L., & Hayes, P. C. (2005a). Kinetics of reduction of FeO from slag by graphite and coal chars. *ISIJ International*, *45*(5), 642–650. https://doi.org/10.2355/isijinternational.45.642

Teasdale, S. L., & Hayes, P. C. (2005b). Observations on the reduction of FeO from slag by graphite, coke and coal char. *ISIJ International*, *45*(5), 634–641.

Terry, B. (1983). The acid decomposition of silicate minerals part I. Reactivities and modes of dissolution of silicates. *Hydrometallurgy*, *10*, 135–150.

Thakurta, J. (2018). Alaskan-type complexes and their associations with economic mineral deposits. In *Processes and Ore Deposits of Ultramafic-Mafic Magmas through Space and Time*. Elsevier Inc. https://doi.org/10.1016/B978-0-12-811159-8.00010-X

U.S.G.S. (2022). *Mineral commodity summaries 2022*. https://pubs.usgs.gov/periodicals/mcs2022/mcs2022-zeolites.pdf

UNCTAD. (2014). Commodities at a glance: Special issue on rare earths. *United Nations Conference on Trade and Development*, *5*, 58.

Verein Deustcher Eisenhüttenleute (Ed.). (1981). *Slag Atlas*. Verlag Stahleisen m.b.H. Düsseldorf.

Villiger, S., Ulmer, P., Müntener, O., & Thompson, A. B. (2004). The liquid line of descent of anhydrous, mantle-derived, tholeiitic liquids by fractional and equilibrium crystallization - An experimental study at 1·0 GPa. *Journal of Petrology*, *45*(12), 2369–2388. https://doi.org/10.1093/petrology/egh042

Voßenkaul, D., Birich, A., Müller, N., Stoltz, N., & Friedrich, B. (2017). Hydrometallurgical processing of eudialyte bearing concentrates to recover rare earth elements via low-temperature dry digestion to prevent the silica gel formation. *Journal of Sustainable Metallurgy*, *3*(1), 79–89. https://doi.org/10.1007/s40831-016-0084-2

Vyazovkin, S., Burnham, A. K., Criado, J. M., Pérez-Maqueda, L. A., Popescu, C., & Sbirrazzuoli, N. (2011). ICTAC Kinetics Committee recommendations for performing kinetic computations on thermal analysis data. *Thermochimica Acta*, *520*(1–2), 1–19. https://doi.org/10.1016/j.tca.2011.03.034

Walters, A., Lusty, P., Chetwyn, C. and Hill, A. (2011). Rare earth elements. *MineralsUK*, 1–54. https://doi.org/10.2749/222137801796348313

Wang, H., Li, G., Dai, Q., Lei, Y., Zhao, Y., Li, B., Shi, G., & Ren, Z. (2006). Effect of additives on viscosity of LATS refining ladle slag. *ISIJ International*, *46*(5), 637–640.

Wang, W., Pranolo, Y., & Cheng, C. Y. (2011). Metallurgical processes for scandium recovery from various resources: A review. *Hydrometallurgy*, *108*(1–2), 100–108. https://doi.org/10.1016/j.hydromet.2011.03.001

Wang, Z., Li, M. Y. H., Liu, Z. R. R., & Zhou, M. F. (2021). Scandium: Ore deposits, the pivotal role of magmatic enrichment and future exploration. *Ore Geology Reviews*, *128*(December 2020), 103906. https://doi.org/10.1016/j.oregeorev.2020.103906

White, J. F., Lee, J., Hessling, O., & Glaser, B. (2017). Reactions between liquid CaO-SiO2 slags and graphite substrates. *Metallurgical and Materials Transactions B: Process Metallurgy and Materials Processing Science*, *48*(1), 506–515. https://doi.org/10.1007/s11663-016-0788-5

Williams-Jones, A. E., & Vasyukova, O. V. (2018). The economic geology of scandium, the runt of the rare earth element litter. *Economic Geology*, *113*(4), 973–988. https://doi.org/10.5382/econgeo.2018.4579

Wood, S. A., & Samson, I. M. (2006). The aqueous geochemistry of gallium, germanium, indium and scandium. *Ore Geology Reviews*, *28*(1), 57–102. https://doi.org/10.1016/j.oregeorev.2003.06.002

Wu, L., Gran, J., & Sichen, D. (2011). The effect of calcium fluoride on slag viscosity. *Metallurgical and Materials Transactions B: Process Metallurgy and Materials Processing Science*, *42*(5), 928–931. https://doi.org/10.1007/s11663-011-9546-x

Xiaoyang, D. (1996). *Carbothermal reduction of ilmenite and fayalite*. University of Arizona.

Yagmurlu, B., Alkan, G., Xakalashe, B., Schier, C., Gronen, L., Koiwa, I., Dittrich, C., & Friedrich, B. (2019). Synthesis of scandium phosphate after peroxide assisted leaching of iron depleted bauxite residue (red mud) slags. *Scientific Reports*, *9*(1), 1–10. https://doi.org/10.1038/s41598-019-48390-z

Yagmurlu, B., Orberger, B., Dittrich, C., Croisé, G., Scharfenberg, R., Balomenos, E., Panias, D., Mikeli, E., Maier, C., Schneider, R., Friedrich, B., Dräger, P., Baumgärtner, F., Schmitz, M., Letmathe, P., Sakkas, K., Georgopoulos, C., & van den Laan, H. (2021). Sustainable supply of scandium for the EU industries from liquid iron chloride based TiO2 plants. *Materials Proceedings*, *5*(86), 9. https://doi.org/10.3390/materproc2021005086

Yagmurlu, B., Zhang, W., Avdibegovic, D., Regadío, M., Koivula, R., Dittrich, C., Binnemans, K., & Friedrich, B. (2018). Advances on scandium recovery beyond state of the art. *ALTA 2018 Uranium-REE-Lithium Proceedings*, *July*, 85–93.

Yang, Y., Raipala, K., & Holappa, L. (2014). Ironmaking. In *Treatise on process metallurgy* (Vol. 3). Elsevier Ltd. https://doi.org/10.1016/B978-0-08-096988-6.00017-1

Yu, D., Zhu, M., Utigard, T. A., & Barati, M. (2014). TG/DTA study on the carbon monoxide and graphite thermal reduction of a high-grade iron nickel oxide residue with the presence of siliceous gangue. *Thermochimica Acta*, *575*, 1–11. https://doi.org/10.1016/j.tca.2013.10.015

Yuan, L., Zhang, X., Yang, Z., Lu, Y., & Chen, H. (2017). Paleoproterozoic Alaskan-type ultramafic–mafic intrusions in the Zhongtiao mountain region, North China Craton: Petrogenesis and tectonic implications. *Precambrian Research*, *296*, 39–61. https://doi.org/10.1016/j.precamres.2017.04.037

Zakaria, Z., & Kamarudin, S. K. (2021). Advanced modification of scandia-stabilized zirconia electrolytes for solid oxide fuel cells application—A review. *International Journal of Energy Research*, *45*(4), 4871–4887. https://doi.org/10.1002/er.6206

Zhan, W., & Guggenheim, S. (1995). The dehydroxylation of chlorite and the formation of topotactic product phases. *Clays and Clay Minerals*, *43*(5), 622–629. https://doi.org/10.1346/CCMN.1995.0430512

Zhang, B., Xue, X., Huang, X., Yang, H., & Chen, G. (2019). Study on recycling and leching valuable elements from Bayan Obo tailings. *Metallurgical Research & Technology*, *116*(1), 114. https://doi.org/10.1051/metal/2018040

Zhou, K., Teng, C., Zhang, X., Peng, C., & Chen, W. (2018). Enhanced selective leaching of scandium from red mud. *Hydrometallurgy*, *182*(March), 57–63. https://doi.org/10.1016/j.hydromet.2018.10.011

Zhou, Y., Yang, H., Xue, X., & Yuan, S. (2017). Separation and recovery of iron and rare earth from Bayan Obo tailings by magnetizing roasting and (NH4)2SO4 activation roasting. *Metals*, *7*(6), 195. https://doi.org/10.3390/met7060195

# Original publications

I. Kallio, R., Tanskanen, P., & Luukkanen, S. (2021). Magnetic preconcentration and process mineralogical study of the Kiviniemi Sc-enriched ferrodiorite, eastern Finland. *Minerals*, 11, 966. https://doi.org/10.3390/min11090966.

II. Kallio, R., Tanskanen, P., Heikkinen, E.P., Kokkonen, T., Luukkanen, S., & Fabritius, T. (2022). Reduction characteristics of Kiviniemi ferrous scandium concentrate. *Minerals Engineering*, 177, 107369. https://doi.org/10.1016/j.mineng.2021.107369

III. Kallio, R., Tanskanen, P., Heikkinen, E.P., Kokkonen, T., Luukkanen, S., & Fabritius, T. (2022). Slag modification in reduction of Kiviniemi ferrous scandium concentrates. *Metals*, 12, 709. https://doi.org/ 10.3390/met12050709

IV. Kallio, R., Lassi, U., Kauppinen, T., Holappa, E., Christophliemk, M., Luukkanen, S., Tanskanen, P., & Fabritius, T. (2022) Leaching characteristics of Sc-enriched, Fe-depleted acidic slags. *Minerals Engineering, 189*, 107901. https://doi.org/10.1016/j.mineng.2022.107901.



Original publications are not included in the electronic version of the dissertation.

838. Hannula, Jaakko (2022) Effect of niobium, molybdenum and boron on the mechanical properties and microstructures of direct quenched ultra-high-strength steels

839. Rajaniemi, Kyösti (2022) Electrocoagulation in water treatment : continuous versus batch processes and sludge utilization

840. Ramezanipour, Iran (2022) Hybrid spectrum mechanism for energy vertical

841. Saukko, Laura (2022) Managing integration capabilities in collaborative inter-organizational projects

842. Tiensuu, Henna (2022) Modelling the quality of the steel products under challenging measurement conditions

843. Avsievich, Tatiana (2022) Red blood cells and novel nanomaterials : towards nanosafety and nanomedicine

844. Wu, Xiaoting (2022) Machine learning for audio-visual kinship verification

845. Pérez Centeno, Víctor (2022) Merging neuroscience technologies in entrepreneurship research

846. Cajander, Niko (2022) Temporary agency work and worker well-being at restaurants : insights into socially sustainable work

847. Nouri, Parisa (2022) Cooperative diversity mechanisms for critical machine-type communications

848. Afonin, Nikita (2022) Development of passive seismic interferometry to study shallow subsurface structure

849. Sdobnov, Anton (2022) Laser speckle contrast imaging for functional visualization

850. Tampio, Kari-Pekka (2022) Enhancing value creation at the front-end of a collaborative hospital construction project

851. Annunen, Petteri (2022) Industrialization in construction : a process model for capability creation

852. Omodara, Linda (2022) Developing and testing sustainability assessment tools for chemical processes and products : case study on critical rare earth elements

853. Karimidastenaei, Zahra (2022) The potential of unconventional water in limiting water scarcity

Book orders:
Virtual book store
http://verkkokauppa.juvenesprint.fi

UNIVERSITY OF OULU P.O. Box 8000 FI-90014 UNIVERSITY OF OULU FINLAND

# ACTA UNIVERSITATIS OULUENSIS



UNIVERSITY OF OULU

ISBN 978-952-62-3492-2 (Paperback)
ISBN 978-952-62-3493-9 (PDF)
ISSN 0355-3213 (Print)
ISSN 1796-2226 (Online)